A Eulerian level set/vortex sheet method for two-phase interface dynamics

M. Herrmann

Center for Turbulence Research, Stanford University, Stanford CA 94305-3035, USA

Abstract

A Eulerian fixed grid approach to simulate the dynamics of two-phase interfaces in the presence of surface tension forces is presented. This level set/vortex sheet method consists of a simplified system of equations that contain individual source terms describing the relevant physical processes at the phase interface explicitly. Hence, this approach provides a framework that will allow for a simplified subsequent modeling of phase interface dynamics in turbulent environments. In the presented level set/vortex sheet method, the location and the motion of the phase interface are captured by a level set equation. Topological changes of the interface, like breakup or merging, are thus handled automatically. Assuming that all vorticity is concentrated at the phase interface, the phase interface itself constitutes a vortex sheet with varying vortex sheet strength. The Eulerian transport equation for the vortex sheet strength is derived by combining its Lagrangian formulation with the level set equation. The resulting differential equation then contains source terms accounting for the stretching of the interface and the influence of surface tension, thus allowing for a detailed study of each effect individually. The results of three test problems, namely the roll-up of a vortex sheet without surface tension, the growth of the Kelvin–Helmholtz instability in the linear regime, and the long-time evolution of the Kelvin–Helmholtz instability are presented.
© 2004 Elsevier Inc. All rights reserved.

Keywords: Two-phase flow; Level set; Vortex sheet; Kelvin–Helmholtz instability

1. Introduction

The disintegration of a liquid jet or sheet into individual small drops can be divided into two consecutive stages, the primary and the secondary atomization. The initial breakup of the liquid jet or sheet into large

---

and small cohesive structures is called primary atomization, whereas the subsequent breakup of these individual structures into ever smaller drops is called secondary atomization.

Usually, the atomization process occurs in a turbulent environment, involving a wide range of time and length scales. Given today's computational resources, the direct numerical simulation of the turbulent breakup process as a whole, resolving all physical processes fully, is impossible, except for some specific, simple applications. Therefore, models describing the physics of the atomization process at the numerically non-resolvable scales have to be employed instead.

A wide variety of models has already been developed for the secondary breakup process. Here, the predominant liquid structures can be assumed to be of simple geometrical shape, like spheres or ellipsoids. The interaction between these structures and the surrounding fluid can thus easily be taken into account and statistical models describing the secondary breakup process in turbulent environments can be derived [1–5].

However, the assumption of simple geometrical shape does not hold true for the primary breakup process, since here, the interface can assume any arbitrary shape. In this case, one potential approach is to start off from a fully resolved description of the interface dynamics using the Navier–Stokes equations that include an additional source term in the momentum equations due to surface tension forces [6]. Usually, the Navier–Stokes equations are then coupled to one of various possible tracking methods in order to track the location, motion, and topology of the phase interface, as for example marker particles [7–9], the volume-of-fluid method [10–12], or the level set method [13–15]. To overcome the computational limitations of a direct numerical simulation of the primary breakup process, ensemble averaging or spatial filtering has to be introduced, resulting in unclosed terms that require modeling [16,17]. Unfortunately, the derivation of such closure models is not straightforward and hence has not been achieved yet. This is in part due to the fact that, with the exception of the surface tension term, all other physical processes occurring at the phase interface itself, like for example stretching, are not described by explicit terms, but rather are hidden within the interdependence of the individual equations. Thus, a formulation containing these terms explicitly could greatly facilitate any attempt to derive the appropriate closure models.

To this end, a novel Eulerian level set/vortex sheet approach is proposed. Within the scope of this method, it is assumed that the effect of the viscous boundary layers adjacent to the phase interface can be neglected. All vorticity is thus concentrated at the phase interface. Hence, the phase interface itself constitutes a vortex sheet.

Usually, vortex sheets are solved by a boundary integral method within a Lagrangian framework where the phase interface is tracked by marker particles, see for example [18–22]. Marker particles allow for highly accurate tracking of the phase interface motion in a direct numerical simulation. However, the introduction of ensemble averaging and spatial filtering of the interface topology is not straightforward and a strategy for the derivation of closure models is not directly apparent. Level sets, on the other hand, have been successfully used in the derivation of closure models in the field of premixed turbulent combustion [23,24]. Thus, to facilitate subsequent modeling approaches of the turbulent phase interface dynamics, here, the phase interface location and motion are tracked by a level set approach.

The combination of vortex sheets and level sets in a Eulerian framework has been demonstrated in the past [25,26]. There, however, surface tension forces have not been taken into account and a transport equation for only the unnormalized vortex sheet strength has been employed, resulting in a simple passive scalar advection equation. Again, the physical processes at the phase interface are described not by explicit source terms, but rather by the interdependence of the level set and the unnormalized vortex sheet strength equations.

Therefore, in the approach presented in this paper, a transport equation for the normalized vortex sheet strength is derived. Thus, the effect of surface tension forces and all other relevant physical processes occur as individual source terms. The coupling of the proposed level set/vortex sheet method to an external turbulent flow field can then provide a framework for the detailed study of these terms in a turbulent environment, resulting in a novel approach to derive closure models for the turbulent primary atomization process.

This paper is divided into four parts. First, the governing equations for the transport of the normalized vortex sheet strength and the level set scalar are derived. Then, the numerical methods applied to solve the level set/vortex sheet approach are presented, followed by the results of three test problems, namely the roll-up of a vortex sheet without surface tension forces, the growth of the Kelvin–Helmholtz instability in the linear regime, and the long-time evolution of the Kelvin–Helmholtz instability. Finally, conclusions are drawn.

2. Governing equations

To simplify the following derivations and discussion, we will limit ourselves to the two-dimensional case. The extension to three dimensions is straightforward.

The focus of this paper is the motion of the phase interface Γ between two inviscid, incompressible fluids, as shown in Fig. 1. In this case, the velocity **u** on either side i of the interface Γ is determined by the incompressible Euler equations given here in dimensionless form as

$$\nabla \cdot \mathbf{u}_i = 0, \tag{1}$$

$$\frac{\partial \mathbf{u}_i}{\partial t} + (\mathbf{u}_i \cdot \nabla)\mathbf{u}_i = -\frac{1}{\rho_i}\nabla p, \tag{2}$$

where ρ is the density and p is the pressure. In addition, the boundary conditions at the interface Γ,

$$[(\mathbf{u}_1 - \mathbf{u}_2) \cdot \mathbf{n}]|_\Gamma = 0, \quad [(\mathbf{u}_1 - \mathbf{u}_2) \cdot \mathbf{t}]|_\Gamma = \eta, \tag{3}$$

$$[p_2 - p_1]|_\Gamma = \frac{1}{We}\kappa \tag{4}$$

and at the far field,

$$\lim_{y \to \pm\infty} \mathbf{u}_i = \begin{pmatrix} U_{\pm\infty} \\ 0 \end{pmatrix}, \tag{5}$$

have to be fulfilled. Here, **n** and **t** are the interface normal and tangential vector, η is the so-called vortex sheet strength, $We = \rho_{\mathrm{ref}}L_{\mathrm{ref}}u_{\mathrm{ref}}^2/\Sigma$ is the Weber number, Σ is the surface tension coefficient, ρ_{ref}, u_{ref}, and L_{ref} are reference density, velocity, and length, respectively, and κ is the local curvature of Γ. An interface subjected to the above boundary conditions is called a vortex sheet, see for example [27]. Parameterizing the interface location by
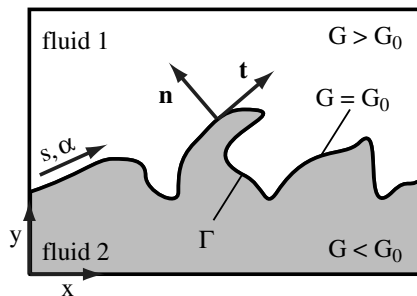

Fig. 1. Interface definition.

$$\mathbf{x}(\alpha,t)|_\Gamma = \begin{pmatrix} x(\alpha,t) \\ y(\alpha,t) \end{pmatrix}\bigg|_\Gamma, \tag{6}$$

the velocity $\mathbf{u}$ at a point $\mathbf{x}$ away from the interface is given by

$$\mathbf{u}(\mathbf{x},t) = \int_\Gamma \eta^*(\alpha,t)\mathbf{e}_z \times \frac{\mathbf{x} - \mathbf{x}(\alpha,t)}{|\mathbf{x} - \mathbf{x}(\alpha,t)|^2}\,d\alpha, \tag{7}$$

where $\mathbf{e}_z$ is the unit vector in the third dimension and η^* is the unnormalized vortex sheet strength defined as

$$\eta^* = \eta\frac{\partial s}{\partial \alpha}, \tag{8}$$

with the arc length metric

$$\frac{\partial s}{\partial \alpha} = \sqrt{\left(\frac{\partial x}{\partial \alpha}\right)^2 + \left(\frac{\partial y}{\partial \alpha}\right)^2}. \tag{9}$$

The evolution equation for the unnormalized vortex sheet strength can be derived by introducing velocity potentials into the Euler equations, Eqs. (1) and (2), and combining the result with the boundary conditions at the interface, Eqs. (3) and (4), see for example [18,19,28]. The Lagrangian formulation for the evolution of a vortex sheet with surface tension then reads

$$\frac{\partial \mathbf{x}(\alpha,t)}{\partial t} = \mathbf{u}_\Gamma, \tag{10}$$

$$\frac{\partial \eta^*(\alpha,t)}{\partial t} = \frac{1}{We}\frac{\partial \kappa}{\partial \alpha}. \tag{11}$$

Here, $\mathbf{u}_\Gamma$ is the velocity at the interface calculated from the principal value integration of Eq. (7). For simplicity, the density of both fluids is assumed to be equal in the above equations.

To derive the Eulerian formulation of the above set of Lagrangian equations, the interface location is first represented by the iso-surface of a scalar field $G(\mathbf{x},t)$. Setting

$$G(\mathbf{x},t)|_\Gamma = G_0 = \text{const.}, \tag{12}$$

$G(\mathbf{x},t) > G_0$ in fluid 1, and $G(\mathbf{x},t) < G_0$ in fluid 2, see Fig. 1, an evolution equation for the scalar G can be derived by simply differentiating Eq. (12) with respect to time and using Eq. (10),

$$\frac{\partial G}{\partial t} + \mathbf{u}\cdot\nabla G = 0, \quad \mathbf{u}(G = G_0) = \mathbf{u}_\Gamma. \tag{13}$$

This equation is called the level set equation and goes back to Osher and Sethian [13]. Strictly speaking, Eq. (13) is valid only at the location of the interface and is independent of the value of G away from the interface. To facilitate the numerical solution of Eq. (13), G is usually chosen to be a distance function away from the interface, i.e.

$$|\nabla G||_{G\neq G_0} = 1. \tag{14}$$

Second, transforming Eq. (11) to a Eulerian formulation results in

$$\frac{\partial \eta^*}{\partial t} + \mathbf{u}\cdot\nabla\eta^* = \frac{1}{We}\frac{\partial s}{\partial \alpha}\nabla\kappa\cdot\mathbf{t}. \tag{15}$$

Making use of the level set scalar G, the interface tangential vector $\mathbf{t}$, normal vector $\mathbf{n}$, and curvature κ can be expressed as

$$\mathbf{t} = \frac{1}{|\nabla G|}\begin{pmatrix} \partial_y G \\ -\partial_x G \end{pmatrix}, \quad \mathbf{n} = \frac{\nabla G}{|\nabla G|}, \tag{16}$$

$$\kappa = \nabla \cdot \mathbf{n} = \nabla \cdot \frac{\nabla G}{|\nabla G|}. \tag{17}$$

Again, Eq. (15) has physical meaning only at the location of the interface itself, that is $G = G_0$, since only there the surface tension term on the right-hand side is defined. Also, as is the case for the level set scalar G, a reinitialization operation for values away from the interface would have to be prescribed.

As has been pointed out by Peng et al. [26], the unnormalized vortex sheet strength η^* in itself does not directly have a physical meaning, since, according to Eq. (3), only $\eta = \eta^*/\partial_\alpha s$ represents a physical quantity, namely the jump in tangential velocity at the interface. It will be shown below that $\partial_\alpha s$ is proportional to $|\nabla G|$, thus any change of $|\nabla G|$, for example by the reinitialization condition, Eq. (14), requires a resetting operation of η^*. This resetting operation has been neglected in [25], but has been employed in [26]. Here, we will derive a transport equation for the jump of the tangential velocity at the interface, i.e. the normalized vortex sheet strength η. This approach has two advantages. On the one hand, since η is independent of $|\nabla G|$, no resetting operation of η is necessary. On the other hand, the transport equation for η contains individual source terms related to the physical processes at the phase interface.

To derive the transport equation for the vortex sheet strength η, an equation for the arc length metric has to be derived, cp. Eq. (8). To achieve this, the arc length metric is first expressed in terms of the level set scalar G. Following the arguments by Harabetian and Osher [29], let us introduce a function ϕ, such that the pair (G, ϕ) forms an orthogonal coordinate system near $G = G_0$,

$$\phi(\mathbf{x}(\alpha), t) = \alpha. \tag{18}$$

Differentiating the level set scalar definition

$$G(\mathbf{x}(\alpha), t) = G_0 \tag{19}$$

and Eq. (18) with respect to α and solving the resulting system leads to

$$\frac{\partial \mathbf{x}}{\partial \alpha} = \frac{1}{J}\begin{pmatrix} -\partial_y G \\ \partial_x G \end{pmatrix}, \tag{20}$$

where J is the Jacobian of (G, ϕ),

$$J = \partial_x G \partial_y \phi - \partial_y G \partial_x \phi. \tag{21}$$

Inserting Eq. (20) into Eq. (9) and introducing $\sigma = |\nabla G|\big|_{G=G_0}$ results in

$$\frac{\partial s}{\partial \alpha} = \frac{1}{|J|}\sigma. \tag{22}$$

For the case analyzed here, the transport equation for J, derived in [29], reduces to

$$\frac{\partial J}{\partial t} + \mathbf{u} \cdot \nabla J = 0. \tag{23}$$

The evolution equation for σ can be derived by applying the ∇ operator to Eq. (13) and multiplying the resulting equation with $\mathbf{n} = \nabla G/|\nabla G|$, which yields

$$\frac{\partial \sigma}{\partial t} + \mathbf{u} \cdot \nabla \sigma = -(\mathbf{n} \cdot \nabla \mathbf{u} \cdot \mathbf{n})\sigma. \tag{24}$$

Then, combining this equation with Eqs. (8), (15), (22), and (23) gives, after some algebraic manipulations, the transport equation for the vortex sheet strength η,

$$\frac{\partial \eta}{\partial t} + \mathbf{u} \cdot \nabla \eta = (\mathbf{n} \cdot \nabla \mathbf{u} \cdot \mathbf{n})\eta + \frac{1}{We}\nabla\kappa \cdot \mathbf{t}. \tag{25}$$

Here, the terms on the left-hand side describe temporal change and convective transport, respectively. The first term on the right-hand side, S, describes the effect of stretching of the vortex sheet and the second term, T, accounts for the influence of surface tension. Note that the above equation is valid only at the interface location itself. To facilitate the numerical solution, a redistribution of η from the interface to the rest of the computational domain is performed by solving

$$\nabla\eta \cdot \nabla G = 0. \tag{26}$$

This sets $\eta = \eta|_{G=G_0} = $ const. in the interface normal direction.

Finally, to close the system of Eqs. (13) and (25), the velocity $\mathbf{u}$ has to be calculated from a line integral of the vortex sheet strength η by introducing Eq. (8) into Eq. (7), yielding

$$\mathbf{u}(\mathbf{x},t) = \int_\Gamma \eta(s,t)\mathbf{e}_z \times \frac{\mathbf{x} - \mathbf{x}(s,t)}{|\mathbf{x} - \mathbf{x}(s,t)|^2}\,\mathrm{d}s. \tag{27}$$

For vortex sheets of length L that are periodic in the x-direction, following Milne-Thomson [30], Eq. (27) can be transformed to

$$u(x,y) = \frac{1}{2}\int_0^L \eta(s)\frac{\sinh 2\pi(y - y(s))}{\cosh 2\pi(y - y(s)) - \cos 2\pi(x - x(s)) + \mu^2}\,\mathrm{d}s, \tag{28}$$

$$v(x,y) = \frac{1}{2}\int_0^L \eta(s)\frac{\sin 2\pi(x - x(s))}{\cosh 2\pi(y - y(s)) - \cos 2\pi(x - x(s)) + \mu^2}\,\mathrm{d}s. \tag{29}$$

Here, the problem that the integral can become singular for $\mathbf{x} \to \mathbf{x}(s)$ is avoided by adding a positive constant μ^2 to the denominator as proposed by Krasny [31].

The above approach for calculating the vortex sheet induced velocity $\mathbf{u}$ has one computational drawback. It requires the evaluation of a complete line integral for each point in the computational domain and is thus very time consuming. Alternatively, a vortex-in-cell type approach [32] can be followed to calculate $\mathbf{u}$.

First, let ψ be the stream function given by

$$\triangle\psi(\mathbf{x}) = \omega(\mathbf{x}), \tag{30}$$

where the vorticity ω is defined by

$$\omega(\mathbf{x}) = \int_\Gamma \eta^*(\alpha)\delta(\mathbf{x} - \mathbf{x}(\alpha))\mathrm{d}\alpha = \int_\Gamma \eta(s)\delta(\mathbf{x} - \mathbf{x}(s))\mathrm{d}s \tag{31}$$

and δ is the delta function [33]. Noting that any surface integral along $G = G_0$ can be transformed to a volume integral by

$$\int_\Gamma f(s)\mathrm{d}s = \int_V f(\mathbf{x}')\delta(G(\mathbf{x}') - G_0)|\nabla G(\mathbf{x}')|\mathrm{d}\mathbf{x}'. \tag{32}$$

Eq. (31) can be rewritten as

$$\omega(\mathbf{x}) = \int_V \eta(\mathbf{x}')\delta(\mathbf{x} - \mathbf{x}')\delta(G(\mathbf{x}') - G_0)|\nabla G(\mathbf{x}')|\mathrm{d}\mathbf{x}'. \tag{33}$$

The vortex sheet induced velocity can then simply be calculated from

$$\mathbf{u}(\mathbf{x}) = \int_V \delta(\mathbf{x} - \mathbf{x}')(\partial_y\psi(\mathbf{x}'), -\partial_x\psi(\mathbf{x}'))^{\mathrm{T}}\mathrm{d}\mathbf{x}'. \tag{34}$$

To summarize, the level set equation (13) and the transport equation for the vortex sheet strength (25) together with either Eq. (27) or Eq. (34) form the system of Eulerian equations describing the dynamics of phase interfaces in the presence of surface tension forces.

3. Numerical methods

The system of equations describing the phase interface dynamics are solved on an equidistant, Cartesian grid. However, instead of solving the equations throughout the whole computational domain, a tube approach is employed to significantly speed up the computations. Following arguments by Peng et al. [26], five distinct tubes around the $G = G_0$ level set, called $\mathscr{I}$-, $\mathscr{I}_2$-, $\mathscr{B}$-, $\mathscr{T}$-, and $\mathscr{N}$-tube are introduced. The condition for a grid node (i,j) to belong to one or more specific tubes is given by

$$(i,j) \in \begin{cases} \mathscr{I} & \text{if } |G_{i,j}| \leqslant \alpha_I\Delta x, \\ \mathscr{I}_2 & \text{if } |G_{i,j}| \leqslant 2\alpha_I\Delta x, \\ \mathscr{B} & \text{if } |G_{i,j}| \leqslant \alpha_B\Delta x, \\ \mathscr{T} & \text{if } |G_{i,j}| \leqslant \alpha_T\Delta x, \\ \mathscr{N} & \text{if any } (i_0,j_0) \in \mathscr{T} \text{ with } i_0 \in [i-3, i+3], \; j_0 \in [j-3, j+3], \end{cases} \tag{35}$$

with Δx being the grid size and typically $\alpha_I = 4$, $\alpha_B = \alpha_I + 3$, and $\alpha_T = \alpha_B + 3$. The use of the respective tubes will be discussed in the following sections.

3.1. Convective terms

The level set equation (13) is a Hamilton–Jacobi equation. In this work, the third-order WENO scheme for Hamilton–Jacobi equations of Jiang and Peng [34] is used. A Roe flux with local Lax–Friedrichs entropy correction (Roe-LLF) [35,36] is employed to solve both the level set equation (13) and the convective term of the η-equation (25). Integration in time is performed by the third-order TVD Runge–Kutta time discretization of Shu [37].

Solution of the convective terms is restricted to the $\mathscr{T}$-tube, where, as suggested by Peng et al. [26], $\mathbf{u}$ in Eqs. (13) and (25) is replaced by

$$\mathbf{u}_{\mathrm{cut}} = c(G)\mathbf{u} \tag{36}$$

with the cut-off function

$$c(G) = \begin{cases} 1, & \alpha_G \leqslant \alpha_B, \\ \frac{(\alpha_G-\alpha_T)^2(2\alpha_G+\alpha_T-3\alpha_B)}{(\alpha_T-\alpha_B)^3}, & \alpha_B < \alpha_G \leqslant \alpha_T, \\ 0, & \alpha_G > \alpha_T, \end{cases} \tag{37}$$

and $\alpha_G = |G|/\Delta x$. This ensures that no artificial oscillations are introduced at the $\mathscr{T}$-tube boundaries.

3.2. Source terms

Both the stretching term S as well as the surface tension term T in the η-equation (25) are integrated in time within the convective TVD Runge–Kutta scheme. Since the source terms have physical meaning only

at the interface itself, their evaluation is limited to the $\mathscr{I}$-tube. For numerical reasons, these values are then redistributed to the $\mathscr{N}$-tube by solving

$$\nabla S \cdot \nabla G = 0, \qquad \nabla T \cdot \nabla G = 0. \tag{38}$$

3.3. Reinitialization

The reinitialization procedure employed here to solve Eq. (14) has originally been proposed by Sussman et al. [14], where the Hamilton–Jacobi type equation

$$\frac{\partial H(\mathbf{x}, t^*)}{\partial t^*} + S(H(\mathbf{x}, t^*))(|\nabla H(\mathbf{x}, t^*)| - 1) = 0, \quad (i, j) \in \mathscr{N}, \tag{39}$$

$$H(\mathbf{x}, t^* = 0) = G(\mathbf{x}, t) - G_0, \tag{40}$$

is solved until

$$||H(\mathbf{x}, t^*) - H(\mathbf{x}, t^* - \Delta t^*)||_\infty < \epsilon_1, \quad (i, j) \in \mathscr{B} \tag{41}$$

with typically $\epsilon_1 = 10^{-3} \Delta x$. In Eq. (39), $S(H)$ is an approximation to the sign function. As pointed out by Peng et al. [26], the proper choice of this approximation is crucial to minimize undesired movement of the $H(\mathbf{x}, t^*) = 0$ interface while solving Eq. (39). Here, we will use the approximated sign function [26]

$$S(H) = \frac{H}{\sqrt{H^2 + |\nabla H|^2 (\Delta x)^2}} \tag{42}$$

with a second-order central difference approximation for ∇H. Eq. (39) is solved by the third-order WENO scheme, cp. Section 3.1, but employing a Godunov flux function instead of the Roe-LLF flux function. Again, the solution in time is advanced by a third-order TVD Runge–Kutta scheme.

Reinitialization is limited to the $\mathscr{N}$-tube which is three cells larger in each direction than the $\mathscr{T}$-tube. In [26], an extension of the $\mathscr{T}$-tube by only one cell in each direction was proposed. However, it was found that this still might introduce fluctuations in the solution, hence an extension by three cells is employed here. The convergence criterium, Eq. (41), is evaluated within the $\mathscr{B}$-tube only.

3.4. Level set correction methods

It is well known that the reinitialization equation (39) tends to unintentionally move the interface in regions of high curvature of G, that is corners of the interface or regions where two or more interface segments are close to each other, even if higher order WENO schemes are employed. Several different correction methods to overcome this problem have been proposed in the past. Here, we use two different approaches.

The first level set correction method is due to Sussman and Fatemi [38]. It aims to preserve the volume of fluid 1, where $G > G_0$, in each grid cell during reinitialization and will henceforth be called volume correction. Here, we will use their original first-order formulation, see [38] for details.

The second level set correction method is based on a combination of the level set equation with marker particles due to Enright et al. [39]. The basic idea is to use Lagrangian particles to correct the errors in the position of the interface as represented by the level set scalar. Here, we will use the scheme described in detail in [39] with one modification, namely that the velocity of the non-escaped Lagrangian particles $\mathbf{v}_p$ is not the flow velocity at their location $\mathbf{x}_p$, but rather the velocity at the interface location closest to the particle position,

$$\mathbf{v}_p = \mathbf{u}(\mathbf{x}_p - S(G(\mathbf{x}_p) - G_0)(G(\mathbf{x}_p) - G_0)\mathbf{n}(\mathbf{x}_p)). \tag{43}$$

This modification ensures that even in flows with strong normal gradients of the interface tangential velocity, particles are moving in accordance with their closest interface point. This second level set correction method will be denoted as particle correction in the following.

3.5. Redistribution

A Fast Marching method is employed to solve the redistribution Eqs. (26) and (38). Here, we use the standard second-order method as described in detail in [40,41]. Redistribution is performed in the $\mathcal{N}$-tube only.

Employing a Hamilton–Jacobi equation based redistribution as proposed by Peng et al. [26] instead of the Fast Marching method proved to introduce too much undesired tangential transport in the redistributed scalars, η, S, and T. Hence, this method has not been used here.

3.6. Velocity calculation methods

Three different methods, denoted $\mathcal{M}_1$ through $\mathcal{M}_3$, are used to calculate the vortex sheet induced velocity $\mathbf{u}$. Method $\mathcal{M}_1$ is based on the line integral (27), whereas methods $\mathcal{M}_2$ and $\mathcal{M}_3$ are based on the vortex-in-cell type approach, Eqs. (31) and (33), respectively.

3.6.1. Line integral formulation: method $\mathcal{M}_1$

Eq. (27), or, in the case of periodic vortex sheets, Eqs. (28) and (29) are used to calculate the vortex sheet induced velocity $\mathbf{u}$ at every grid point in the $\mathcal{T}$-tube.

To evaluate the line integrals in these equations, the geometric location of the interface $G = G_0$ has to be reconstructed. Grid cells containing part of the interface are easily identified by

$$\neg\left(\min_{i^*\in[i,i+1],j^*\in[j,j+1]} G_{i^*,j^*} > G_0 \vee \max_{i^*\in[i,i+1],j^*\in[j,j+1]} G_{i^*,j^*} < G_0\right). \tag{44}$$

The entry and exit coordinates of the interface into these cells are calculated by approximating G by cubic splines along the grid lines. The interface shape itself is assumed to be a straight line connecting the entry and exit points in each cell. The integration along these line segments is performed by five point Gaussian quadrature, with η at the quadrature points calculated from two-dimensional third-order B-splines. This approach will be denoted as method $\mathcal{M}_1$.

The disadvantage of using method $\mathcal{M}_1$ is the fact that it is computationally expensive, because for each grid node in the $\mathcal{T}$-tube a line integral has to be evaluated. Furthermore, the interface location and topology must be reconstructed, thus loosing in effect one of the benefits of the level set approach. However, method $\mathcal{M}_1$ is highly accurate for $\mu \to 0$ in Eqs. (28) and (29) and is thus used as a reference method in the following.

3.6.2. Vortex-in-cell approach: methods $\mathcal{M}_2$ and $\mathcal{M}_3$

In order to solve the Poisson equation for the stream function, Eq. (30), the vorticity at each grid point in the computational domain has to be calculated by a numerical version of either Eq. (31) or Eq. (33). Approximating the delta function by a smoothed version, the vorticity, theoretically located solely on the interface, is in effect spread out to the neighboring grid nodes. Hence, this approach is similar to the vortex-in-cell method that spreads the vorticity of Lagrangian vortex particles to their surrounding grid nodes [32,33]. Quite a number of spreading functions have been proposed to this end [42]. Here we will use

$$\delta(\mathbf{x} - \mathbf{x}(s)) = \delta_\varepsilon(x - x(s))\delta_\varepsilon(y - y(s)), \tag{45}$$

$$\delta(G(\mathbf{x}') - G_0) = \delta_\varepsilon(G(\mathbf{x}') - G_0), \tag{46}$$

with the numerical delta function δ_ε as proposed by Peskin [43]

$$\delta_\varepsilon(x) = \begin{cases} \frac{1}{2\varepsilon}\left[1 + \cos\left(\frac{\pi x}{\varepsilon}\right)\right], & |x| \leqslant \varepsilon, \\ 0, & |x| > \varepsilon, \end{cases} \tag{47}$$

and the spreading parameter ε set to $\varepsilon = \alpha_I \Delta x$.

If the vorticity is calculated by Eq. (31), the integration along the interface is calculated analogous to method $\mathcal{M}_1$ described in Section 3.6.1, thus requiring the reconstruction of the location and topology of the phase interface from the level set scalar field. Note, however, that in contrast to Eqs. (28) and (29), the integration of Eq. (31) only needs to be performed in the $\mathcal{I}$-tube and can be confined to

$$\omega(\mathbf{x}) = \int_{\Gamma'} \eta(s)\delta(\mathbf{x} - \mathbf{x}(s))\mathrm{d}s, \tag{48}$$

where Γ' is the part of the interface with $|x - x(s)| \leqslant \varepsilon$ and $|y - y(s)| \leqslant \varepsilon$. This approach shall be called method $\mathcal{M}_2$ in the following.

If the vorticity is calculated by Eq. (33), denoted in the following as method $\mathcal{M}_3$, the reconstruction of the interface location and topology as required in method $\mathcal{M}_2$ is avoided. The integration in Eq. (33) is performed by first evaluating

$$\Omega(\mathbf{x}', t) = \eta(\mathbf{x}', t)\delta(G(\mathbf{x}') - G_0)|\nabla G(\mathbf{x}')| \tag{49}$$

for all cells within the $\mathcal{I}$-tube and then integrating

$$\omega(\mathbf{x}, t) = \int_{V'} \delta(\mathbf{x} - \mathbf{x}')\Omega(\mathbf{x}', t)\mathrm{d}\mathbf{x}' \tag{50}$$

for all cells within the $\mathcal{I}_2$-tube by a simple midpoint rule, with V' being the area, where $|x - x'| \leqslant \varepsilon$ and $|y - y'| \leqslant \varepsilon$.

The Laplace equation for the stream function, Eq. (30), is solved by the package FISHPACK [44] throughout the whole computational domain employing appropriate boundary conditions for the stream function ψ.

Finally, the calculation of the vortex sheet induced velocity $\mathbf{u}$ from the stream function, Eq. (34), for both methods $\mathcal{M}_2$ and $\mathcal{M}_3$ is again a two-step process. First, an initial velocity $\mathbf{U}$ is calculated at each grid node by second-order central differences

$$\mathbf{U}_{i,j} = \left(\frac{\psi_{i,j+1} - \psi_{i,j-1}}{2\Delta y}, -\frac{\psi_{i+1,j} - \psi_{i-1,j}}{2\Delta x}\right)^{\mathrm{T}}. \tag{51}$$

Second, in order to be consistent with the spreading step of the vorticity, Eq. (48) or Eq. (33), the same numerical integration method and δ function has to be used in the interpolation step to calculate $\mathbf{u}$,

$$\mathbf{u}(\mathbf{x}, t) = \int_{V'} \delta(\mathbf{x} - \mathbf{x}')\mathbf{U}(\mathbf{x}', t)\mathrm{d}\mathbf{x}', \tag{52}$$

evaluated within the $\mathcal{T}$-tube. Note that Eq. (52) defines a consistent interpolation step only, if the vorticity is calculated by method $\mathcal{M}_2$. Since method $\mathcal{M}_3$ involves an additional delta function of the level set scalar G in Eq. (33), no consistent interpolation step can be defined. Nevertheless, Eq. (52) is still employed as the interpolation step for method $\mathcal{M}_3$.

4. Results

Three different test problems are presented in the following to validate the level set/vortex sheet method proposed in this paper. First, the roll-up of vortex sheets without surface tension forces is discussed. The objective of this test problem is to analyze the desingularization and convergence properties of the level set/vortex sheet method. Furthermore, the different velocity and level set correction methods are compared, and the influence of the delta function spreading parameter ε is analyzed. Second, results of the calculated growth rate of the Kelvin–Helmholtz instability in the linear regime are compared to linear theory in order to evaluate the accuracy of all three velocity methods. Finally, the long-time evolution of the Kelvin–Helmholtz instability for three different Weber numbers is presented.

4.1. Vortex sheet roll-up

4.1.1. Moore singularity

Pure vortex sheets represent a special class of phase interfaces in that no surface tension forces exist. Thus, they do have constant unnormalized vortex sheet strength η^*, cp. Eq. (11). However, pure vortex sheets constitute an ill posed problem, since linear theory predicts that the growth rate of a sinusoidal disturbance of wave number k is proportional to k. Thus, as pointed out by Moore [45], a vortex sheet develops a singularity at some critical time t_c, typically a discontinuity in curvature.

In order to calculate the behavior of the vortex sheet beyond t_c, some form of desingularization has to be introduced, either by replacing the exact equations by desingularized versions, see for example the vortex blob method [31], cp. Eqs. (28) and (29), or by adding physical effects like surface tension forces [19] or viscosity [46].

In the case of the level set/vortex sheet method presented here, desingularization is twofold. For one, all transport equations are solved by a finite difference scheme on an underlying numerical grid, thus all derivatives of finite quantities are inherently limited by the employed grid spacing. Second, the delta functions in methods $\mathscr{M}_2$ and $\mathscr{M}_3$ are approximated by the numerical delta function δ_ε of finite width ε, Eq. (47). Thus, vorticity is not solely located at the interface but spread out to neighboring grid nodes. To some extent, this crudely mimics the effect of viscosity [46], since the shear layer is not of zero thickness as in the inviscid case, but rather has a finite, constant thickness proportional to ε.

In order to provide a first validation of the level set/vortex sheet method, the critical time t_c in the non-desingularized limit is estimated following Krasny [31] by successively reducing the degree of desingularization, i.e. the grid spacing and the spreading parameter. The initial conditions used are those proposed by Meiron et al. [47]. Initially, the vortex sheet is flat and located at $y = 0$ inside a box of size $[0, 2\pi] \times [-\pi, \pi]$ with a sinusoidal disturbance of the vortex sheet strength, $\eta = 1 + a \cos x$ and $a = 0.125$. With these initial conditions, the predicted critical time is $t_c \approx 2.84$ [48]. Three calculations were performed, successively reducing the desingularization, i.e. the grid spacing and the spreading parameter, from $\Delta x = 2\pi/256$ with $\varepsilon = 16/256$, to $\Delta x = 2\pi/512$ with $\varepsilon = 8/256$, and to $\Delta x = 2\pi/1536$ with $\varepsilon = 6/256$.

Fig. 2 shows the distribution of curvature and curvature derivative, $\partial_s \kappa$, along the normalized arclength s/L at two different times close to the critical time t_c. Both the curvature and the curvature derivative distributions clearly show the onset of the Moore singularity at $s/L = 0.5$. Decreasing the desingularization obviously increases the curvature derivative at any given time. However, the $\varepsilon = 6/256$ case shows some small fluctuations of $\partial_s \kappa$ not present in the other two cases. This is due to the fact that a decrease of ε increases the growth rate of higher wave number fluctuations [31]. The initial amplitudes of these higher wave number disturbances are due to the numerical error associated with the employed numerical grid. Obviously, the 1536×1536 grid is barely sufficient to delay the growth of these higher wave number disturbances. A further reduction of ε would thus require a substantially finer grid. Furthermore, at $t = 3.2$ the
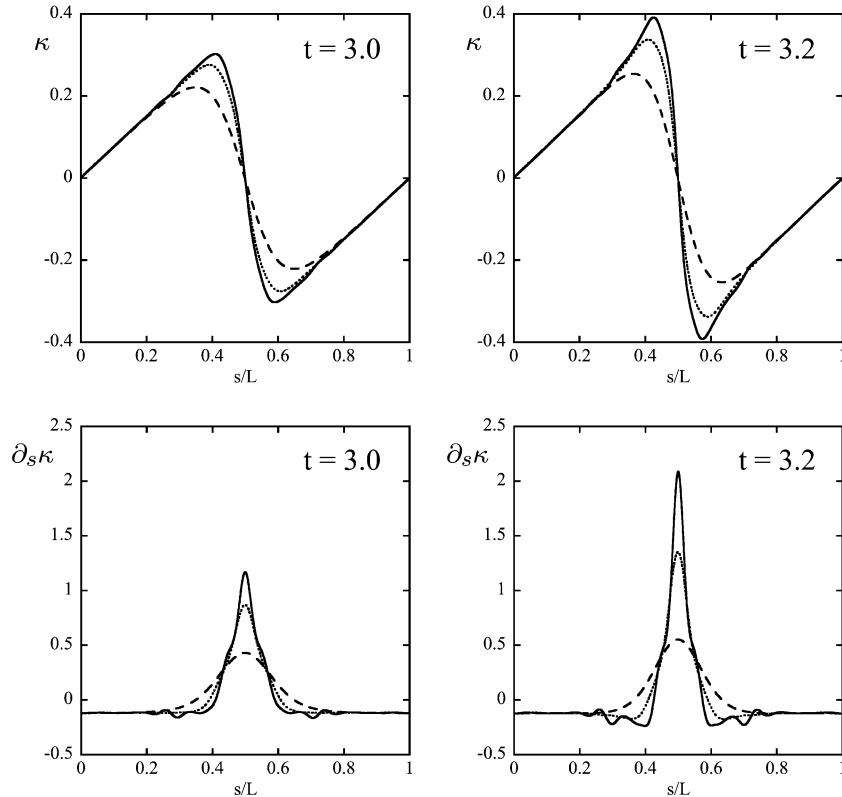
Fig. 2. Vortex sheet curvature (top) and curvature derivative (bottom) at times close to the critical time, $t = 3.0$ (left) and $t = 3.2$ (right) for $\varepsilon = 16/256$ (dashed), $\varepsilon = 8/256$ (dotted), and $\varepsilon = 6/256$ (solid).

$\partial_s\kappa$ distribution for both $\varepsilon = 8/256$ and $\varepsilon = 6/256$ exhibits two local minima directly adjacent to the central maximum. This behavior is consistent with that reported by Shelley [48].

To determine t_c in the non-desingularized limit, the critical time for each of the three calculations is estimated using a procedure proposed by Shelley [48]. The values of $1/\partial_s\kappa$ at $s/L = 0.5$ between $t = 1.0$ and $t = 3.2$ are extrapolated to zero using a third order polynomial that provides an excellent fit to the data points. The resulting critical times are shown in Fig. 3 as a function of the spreading parameter ε. A linear extrapolation is then used to estimate t_c for $\varepsilon \to 0$ and $\Delta x \to 0$, yielding a critical time of $t_c = 3.001$. Although this time is slightly larger than the critical time predicted by theory, it is in excellent agreement with the results of Shelley [48], who estimates $t_c = 3.015$ using a high accuracy point-vortex method.

4.1.2. Evolution beyond the Moore singularity

As discussed in the previous section, the presented method desingularizes the vortex sheet problem such that calculations beyond the Moore singularity are possible. The initial conditions used to study the long-time evolution are similar to those used by Krasny [31]. The initial shape of the interface,

$$x(\alpha, t = 0) = \alpha + A_0 \sin 2\pi\alpha, \tag{53}$$

$$y(\alpha, t = 0) = A_0 \sin 2\pi\alpha, \tag{54}$$

is represented by setting

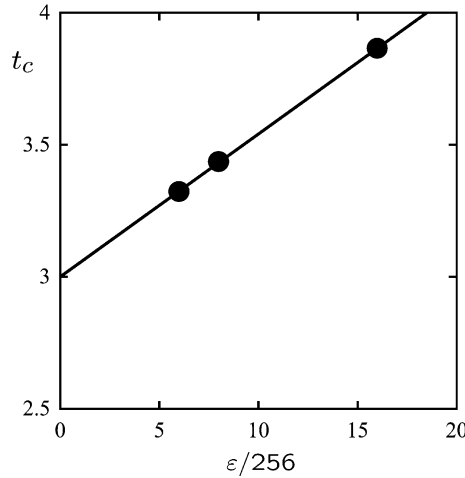Fig. 3. Estimation of critical time.

$$G(\mathbf{x}, t = 0) = y - A_0 \sin\left(\frac{2\pi}{B}\left[x - A_0 \sin\frac{2\pi}{B}x\right]\right), \tag{55}$$

with amplitude $A_0 = 0.01$ and $B = 1$. The initial unnormalized vortex sheet strength is $\eta^* = -1$. Thus, the initial vortex sheet strength can be determined to be

$$\eta_{\mathrm{VS}}(\mathbf{x}, t = 0) = \frac{\eta^*}{\sqrt{1 + \frac{4\pi A_0}{B}\cos\frac{2\pi}{B}x + 2\left[\frac{2\pi A_0}{B}\cos\frac{2\pi}{B}x\right]^2}}. \tag{56}$$

To satisfy Eqs. (14) and (26), a reinitialization and a redistribution step are then performed. Calculations are performed in a box of size $B \times B$ on an equidistant 256×256 Cartesian grid with periodic boundary conditions at the left and right and slip walls at the bottom and top.

Fig. 4 shows the temporal evolution of the vortex sheet calculated with velocity method $\mathcal{M}_2$, particle correction of the level set, and a spreading parameter of $\varepsilon = 16/256$. A vertical slope of the interface is achieved at $t = 0.74$, whereupon roll-up is initiated. The outside shape of the vortex sheet initially is almost circular, but is stretched progressively into a more elliptical shape, while ever more turns are generated in the central core roll-up region.

Fig. 5 shows the vortex sheet strength η, curvature κ, and stretching term S along the interface's normalized arc length s/L at four different times. Here, L denotes the length of the phase interface. The stretching term S is initially positive at both ends of the vortex sheet and negative in the middle part, leading to a decrease of the absolute value of η at both ends of the sheet and an initial increase in the central roll-up region, consistent with the mechanism forming the Moore singularity. This creates a local maximum in the absolute value of η at $s/L = 0.5$, which, although decreasing over time, persists for later times. The visible local variations of S along s/L are due to the change in direction of the interface caused by the roll-up of the vortex sheet. This in turn leads to the local variations of η along s/L. The distribution of the interface curvature clearly shows the discontinuity of κ at $s/L = 0.5$ due to the Moore singularity. However, κ exhibits strong fluctuations in the inner part of the roll-up region, $s/L = 0.4, \ldots, 0.6$, for later times. The reason for this behavior can be attributed to the level set particle correction method and is analyzed in more detail below.
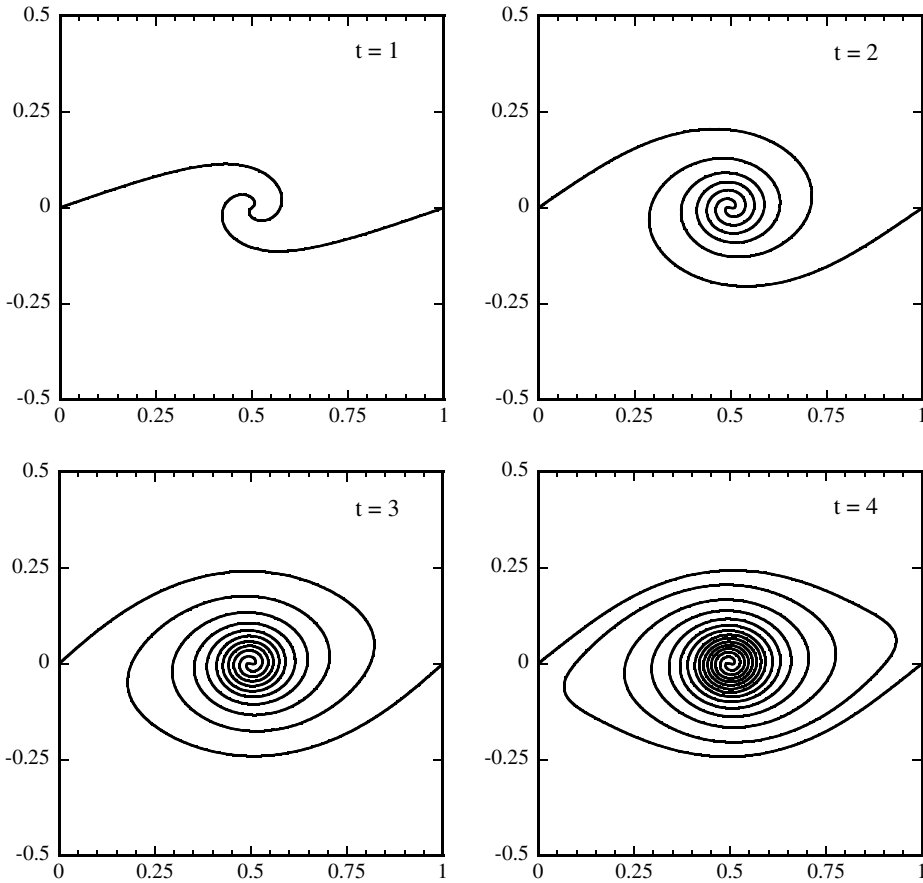
Fig. 4. Vortex sheet shape, 256×256 grid, method $\mathcal{M}_2$, particle correction, $\varepsilon = 16/256$, $t = 1, 2, 3,$ and 4.

Nonetheless, the results obtained here are in excellent agreement with the vortex sheet roll-up reported by Krasny [31], both in terms of the outside shape of the vortex sheet as well as the number of turns generated in the central core region for comparable values of the respective desingularization parameters.

4.1.3. Grid resolution study

In order to demonstrate grid convergence of the solution, Fig. 6 shows the interface shape at $t = 3$ for a constant spreading parameter $\varepsilon = 16/256$ and four different levels of grid resolution. Obviously, a grid resolution of 64×64 is insufficient to support the small scale structures in the inner core region of the roll-up and merging occurs. At a resolution of 128×128, the grid itself is sufficient to avoid merging, however, the interface is rough with small scale wiggles. These are due to the particle level set correction scheme that on the one hand ensures the non-merging of the interface, but does so at the cost of introducing local fluctuations into the interface geometry. At 256×256, the grid resolution is fine enough to avoid most particle corrections and the interface is predominantly smooth. Finally, at 512×512, the interface shape seems very similar to the one at 256×256, the only difference being that due to the increased resolution about one half of an additional turn is generated in the central core.

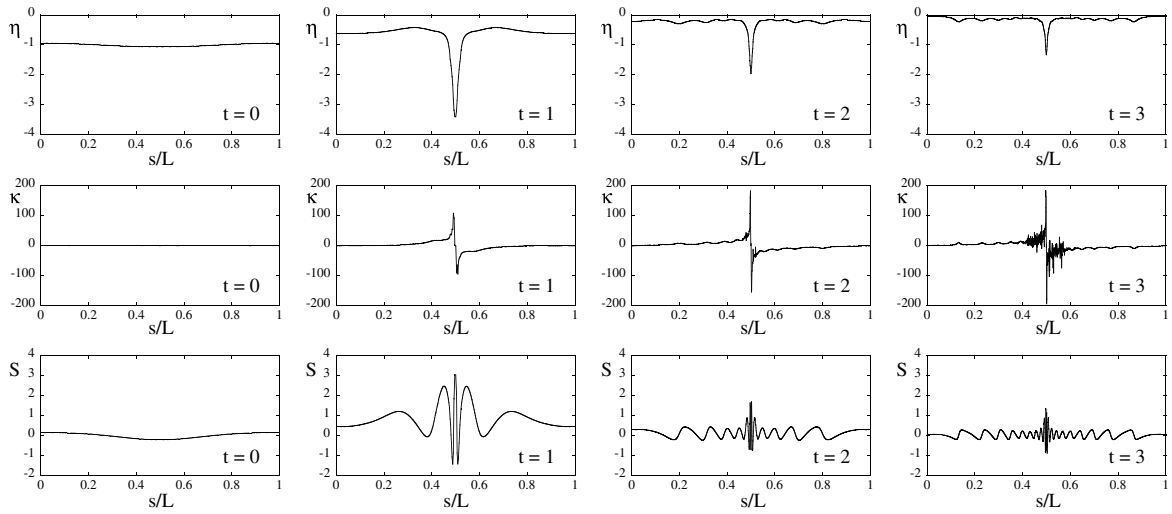Assuming that the 512×512 grid represents the exact solution, Table 1 shows the interface position error E [38],

Fig. 5. Vortex sheet strength η (top), curvature κ (middle), and stretching term S (bottom), 256×256 grid, method $\mathcal{M}_2$, particle correction, $\varepsilon = 16/256$, $t = 0, 1, 2$, and 3.
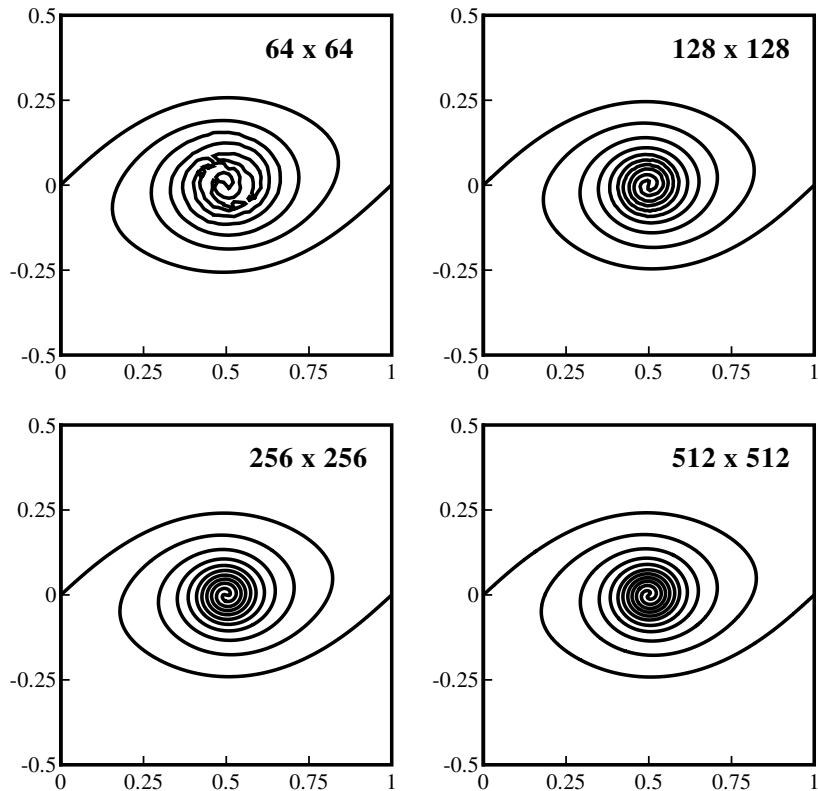

Fig. 6. Grid resolution study, method $\mathcal{M}_2$, particle correction, $\varepsilon = 16/256$, $t = 3$, 64×64, 128×128, 256×256, and 512×512 grid.

Table 1
Interface position error E and order of convergence for vortex sheet roll-up

Grid	$E(t = 1)$	Order	$E(t = 2)$	Order	$E(t = 3)$	Order
64×64	0.0194		0.0469		0.0929	
128×128	0.0074	1.4	0.0220	1.1	0.0369	1.3
256×256	0.0020	1.9	0.0099	1.1	0.0186	1.0

$$E = \int_V |H(G_{512}(\mathbf{x})) - H(G(\mathbf{x}))| d\mathbf{x}, \tag{57}$$

evaluated by partitioning each grid cell into 100×100 subcells, with G calculated by bilinear interpolation. As can be seen, the level set/vortex sheet method achieves slightly better than order one convergence.

4.1.4. Influence of level set correction methods and spreading parameter

The influence of the velocity calculation and level set correction methods is shown in Fig. 7. The top row depicts the shape of the vortex sheet at $t = 3$ calculated with velocity method $\mathcal{M}_2$ without and with one of the two level set correction methods. The bottom row shows the respective results obtained with method $\mathcal{M}_3$. Although the outside shape of the vortex sheet is uninfluenced by the choice of velocity calculation and level set correction methods, the central roll-up region of the vortex sheet exhibits significant differences. Without any level set correction scheme, method $\mathcal{M}_2$ generates more than two additional turns compared to method $\mathcal{M}_3$. This can be ascribed to the transformation from the surface to the volume integral in
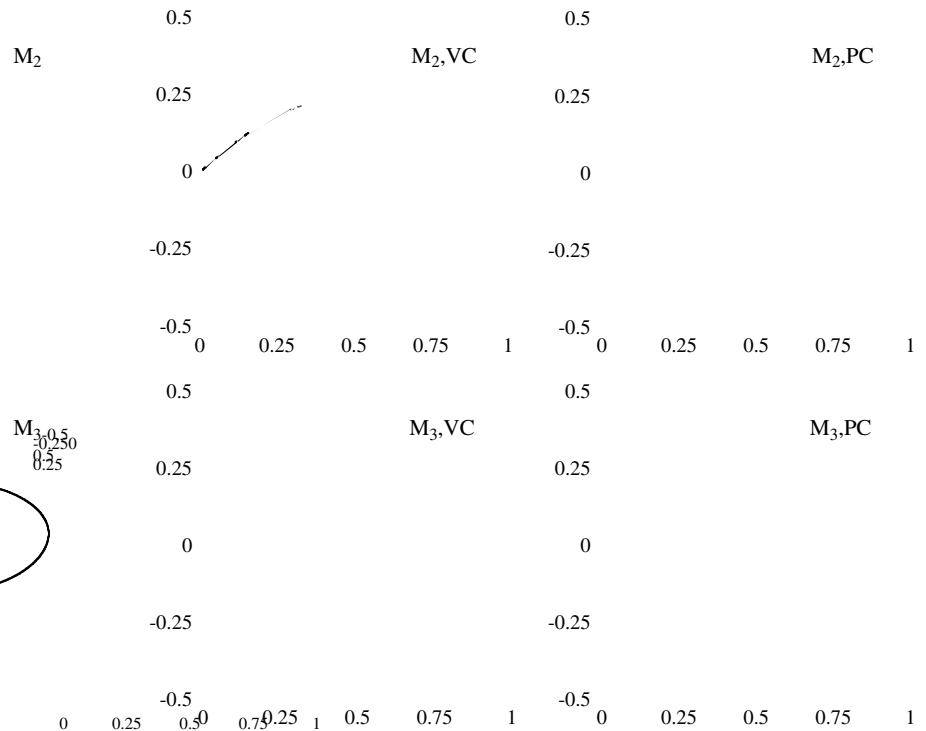

Fig. 7. velocity calculation method at $t = 3$, 256×256 grid, $\varepsilon = 16/256$, method $\mathcal{M}_2$ (top), method $\mathcal{M}_3$ (bottom), no correction volume correction (center), particle correction (right).

Eq. (33), employed in the derivation of method $\mathcal{M}_3$. If two or more interface segments are closer than ε from a given point $\mathbf{x}'$, the numerical delta function $\delta_\varepsilon(G(\mathbf{x}') - G_0)$, Eq. (46), will only take the closest interface segment into account, whereas all other interface segments are incorrectly neglected. This is due to the single valued nature of the level set scalar. In the case of the vortex sheet roll-up, this leads to an under-prediction of the vorticity ω in the central core region for larger times, when the interface segments are less than 2ε apart. This in turn causes the central core velocities to be under-predicted, resulting in the above mentioned underperformance of method $\mathcal{M}_3$ with regard to the number of turns in the central core. Method $\mathcal{M}_2$ on the other hand does not suffer from this problem, because Eq. (45) is not based on a single valued function, but rather on the geometrical distance to each interface segment.

Furthermore, Fig. 7 shows that the application of a level set correction method has hardly any influence on the results when applied in conjunction with method $\mathcal{M}_3$. Since method $\mathcal{M}_3$ produces fewer turns in the central core, adjacent interface segments are still sufficiently far apart as to induce any significant numerical error in the level set advection or reinitialization step that would require correction. However, a significant influence can be discerned when using either one of the level set correction methods in conjunction with method $\mathcal{M}_2$. This is due to the fact that now the interface segments in the central core are so tightly packed that without using any correction, undesired movement of the interface caused by the reinitialization iteration, Eq. (39), prohibits any additional turns. Using the volume correction [38] alleviates part of this problem and one more turn is generated. The particle correction [39] is even more effective, as it generates two additional turns as compared to using no level set correction method at all.

However, both level set correction schemes share one major drawback. Fig. 8 depicts the curvature distribution along the normalized arc length at $t = 3$ for method $\mathcal{M}_2$. Without any level set correction method, the curvature distribution remains smooth and no spurious fluctuation can be discerned. Employing the volume correction method, some small spurious fluctuations in the curvature distribution appear. This results in large fluctuations of the derivative of the curvature needed to calculate the surface tension term T in Eq. (25). Using the particle correction scheme aggravates this behavior, as strong spurious fluctuation can be seen clearly in the curvature distribution. The reason for these fluctuations may be attributed to the local nature of the level set correction methods. Both detection and correction of numerical errors in the level set scalar field are performed only locally. In addition, corrections in the particle correction method are only performed, if a local threshold error is surpassed [39]. Hence, one cell might be corrected, while a neighboring cell is still left untouched resulting in the observed fluctuations in the curvature distribution. To overcome this shortcoming of the correction methods, a non-local correction, keeping the nth derivative of the level set scalar smooth, has to be devised. Within the scope of the presented level set/vortex sheet method, the 3rd derivative of G would have to be kept smooth due to the surface tension term T in the η-equation (25). Since such a non-local correction scheme is presently unavailable, all calculations involving surface tension forces are performed without using any level set correction method at all.

The influence of decreasing the spreading parameter ε is shown in Fig. 9. Here, close-ups of the central core region at $t = 1$ calculated on a 512×512 equidistant grid with velocity method $\mathcal{M}_2$, particle correction
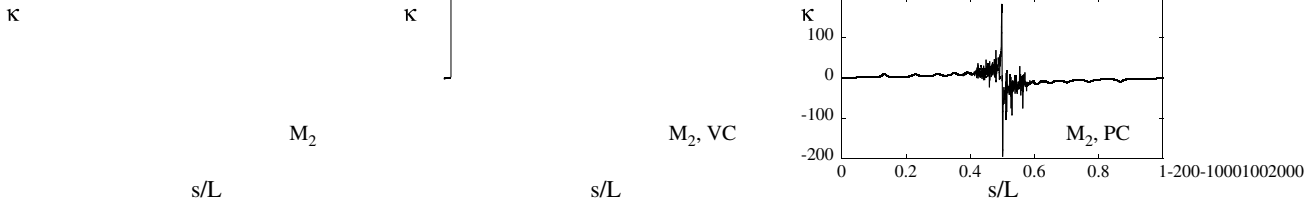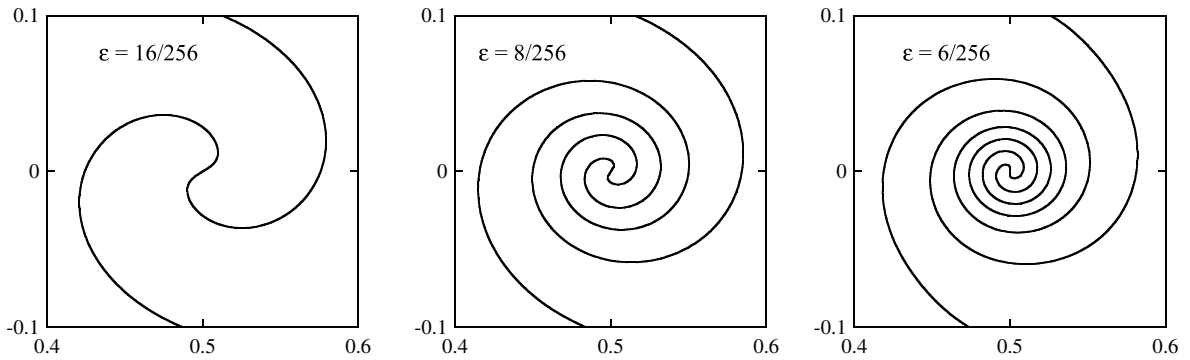
Fig. 9. Influence of the spreading parameter ε at $t = 1$, 512×512 grid, method $\mathcal{M}_2$, particle correction, $\varepsilon = 16/256$ (left), $\varepsilon = 8/256$ (center), $\varepsilon = 6/256$ (right).

and varying ε are shown. Decreasing ε obviously increases the number of generated turns. These results are consistent with those reported by Krasny [31], where a decrease of the desingularization parameter μ in Eqs. (28) and (29) also yielded an increase in the number of turns.

However, as discussed above, decreasing the spreading parameter further to $\varepsilon = 5/256$ results in the noticeable growth of secondary instabilities of higher wave number, as shown in Fig. 10. This is consistent with linear theory, since larger wave number disturbances are associated with higher growth rates. The effect of the spreading parameter ε is thus similar to the effect of the desingularization parameter μ in [31], in that increasing ε decreases the growth rates of these higher wave numbers. Consequently, decreasing ε allows higher wave numbers to grow faster. Note also that at $t = 1$ some interface segments have merged. This is due to the fact that, if two adjacent interface segments enter the same computational grid cell, the single valued level set scalar is unable to resolve both segments simultaneously. Hence, merging of these interface segments occurs automatically.

Finally, Fig. 11 depicts the distribution of curvature along the interface at $t = 0.5$ for decreasing spreading parameters ε. For $\varepsilon \geqslant 8/256$ no secondary instabilities can be discerned. However, some small secondary instabilities are visible for $\varepsilon = 6/256$ and they become of major importance for $\varepsilon = 5/256$. As indicated above, these results are consistent with linear theory.
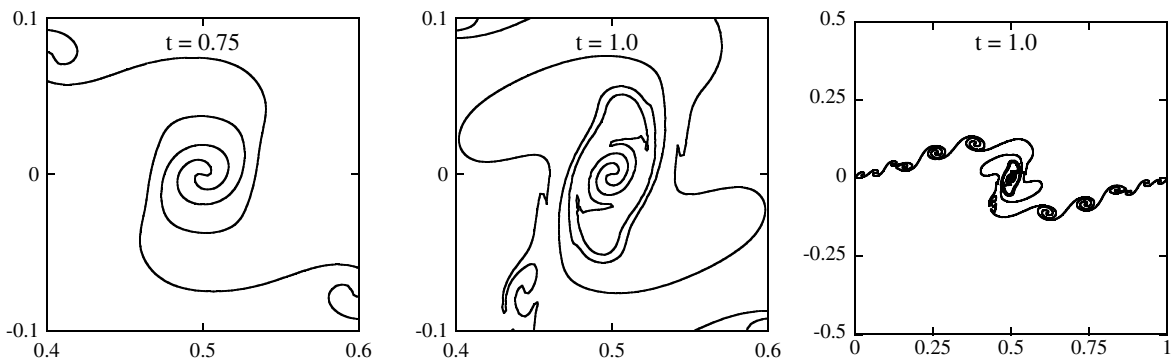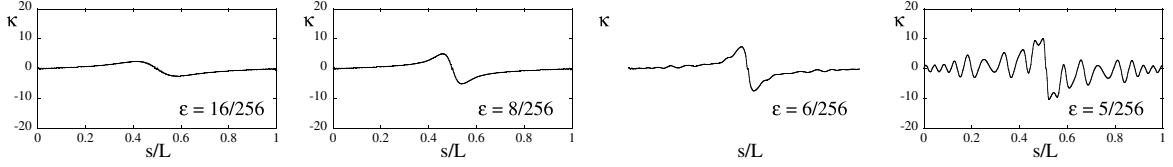

Fig. 10. Influence of the spreading parameter ε, 512×512 grid, method $\mathcal{M}_2$, particle correction, $\varepsilon = 5/256$, $t = 0.75$ closeup (left), $t = 1$ closeup (center), $t = 1$ (right).

4.2. Kelvin–Helmholtz instability in the linear regime

A velocity shear between two fluids can give rise to the so-called Kelvin–Helmholtz instability, if the velocity profile between the two fluids exhibits an inflexion point [49]. This phenomenon was first studied by Helmholtz [50] and Kelvin [51] in the inviscid limit for a shear layer of zero thickness, i.e. a velocity discontinuity. For fluids of equal density, the growth rate w in the linear regime for the unbounded case is

$$w(We) = \frac{k}{2}\sqrt{1 - \frac{2k}{We}}. \tag{58}$$

The case of a shear layer of finite size and constant shear was subsequently analyzed by Rayleigh [49]. In the inviscid and $We = \infty$ limit, the growth rate w in the linear regime becomes

$$w(d) = \frac{k}{2}\sqrt{\frac{e^{-2kd} + 2kd - 1}{(kd)^2} - 1}, \tag{59}$$

with d the shear layer thickness defined as

$$d = \frac{\eta}{(\partial u/\partial y)_{\max}}. \tag{60}$$

Although numerical solutions are possible for arbitrary shear layer velocity profiles [52,53], comparisons will be limited to the above analytical solutions for validation purposes.

The initial conditions for the level set scalar G are given by Eq. (55) with $A_0 = 1 \times 10^{-5}$ and $B = 1$. The initial vortex sheet strength distribution is calculated from

$$\eta(\mathbf{x}, t = 0) = \frac{w(We)}{w(We = \infty)}(\eta_{VS}(\mathbf{x}, t = 0) - \eta^*) + \eta^* \tag{61}$$

with $\eta^* = -1$ and η_{VS} given by Eq. (56). Periodic boundary conditions are employed at the left and right domain boundary whereas slip conditions are used at the lower and upper boundary. This in theory constitutes a bounded shear layer flow. However, the upper and lower boundary are placed sufficiently far away from the interface, as to have no further influence on the presented results, thus allowing comparisons with the theoretical results of the unbounded case. All simulations are performed in a $B \times 2B$ box employing an equidistant 256×512 Cartesian grid.

Fig. 12 compares the growth rates w calculated using the three different velocity calculation methods,

$$w = \frac{1}{t_1} \int_0^{t_1} w(t)\mathrm{d}t, \quad t_1 = 0.5, \tag{62}$$

to the results obtained by linear theory for varying ε, Eq. (58). Table 2 lists the respective numerical values. As expected, the agreement between calculation and theory is best for the reference method $\mathcal{M}_1$, because no numerical spreading function is required to calculate the vortex sheet induced velocity. For the lowest value
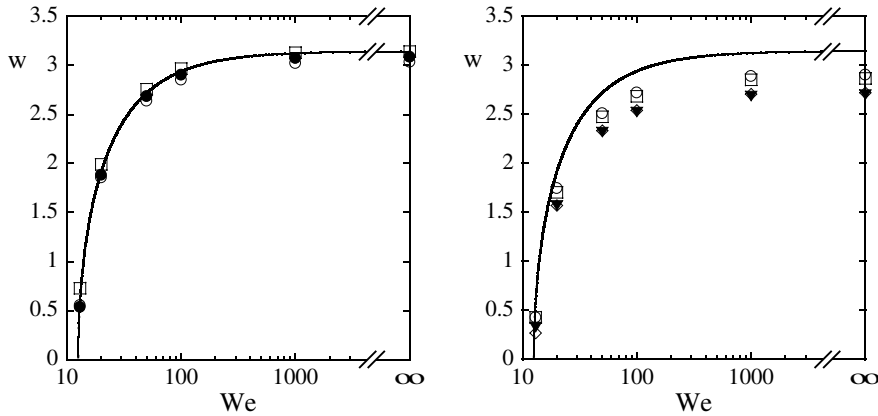
Fig. 12. Growth rate w of the Kelvin–Helmholtz instability in the linear regime, velocity method $\mathcal{M}_1$: $\mu = 0$ (●, left), $\mathcal{M}_2$: $\varepsilon = 4/256$ (○, left), $\mathcal{M}_3$: $\varepsilon = 4/256$ (□, left), $\mathcal{M}_2$: $\varepsilon = 8/256$ (○, right), $\mathcal{M}_3$: $\varepsilon = 8/256$ (□, right), $\mathcal{M}_2$: $\varepsilon = 16/256$ (▼, right), $\mathcal{M}_3$: $\varepsilon = 16/256$ (◇, right), and linear theory (lines).

Table 2
Linear growth rates w of the Kelvin–Helmholtz instability for varying ε and We, 256×512 grid, methods $\mathcal{M}_1$, $\mathcal{M}_2$, and $\mathcal{M}_3$

Method/We	13	20	50	100	1000	∞
Theory	0.574	1.915	2.718	2.938	3.122	3.142
$\mathcal{M}_1$, $\mu = 0$	0.535	1.881	2.685	2.903	3.073	3.084
$\mathcal{M}_2$, $\varepsilon = 4/256$	0.552	1.856	2.638	2.852	3.021	3.034
$\mathcal{M}_3$, $\varepsilon = 4/256$	0.726	1.991	2.756	2.965	3.129	3.140
$\mathcal{M}_2$, $\varepsilon = 8/256$	0.426	1.744	2.505	2.717	2.886	2.899
$\mathcal{M}_3$, $\varepsilon = 8/256$	0.429	1.703	2.472	2.682	2.849	2.863
$\mathcal{M}_2$, $\varepsilon = 16/256$	0.329	1.568	2.316	2.521	2.685	2.698
$\mathcal{M}_3$, $\varepsilon = 16/256$	0.267	1.569	2.332	2.539	2.703	2.717

of the spreading parameter, $\varepsilon = 4/256$, method $\mathcal{M}_2$ slightly under-predicts the linear growth rate by about 3%. This is due to the introduction of the numerical spreading function in Eq. (48) and the consequently theoretically reduced linear growth rate, cp. Eq. (59). Method $\mathcal{M}_3$ on the other hand marginally overpredicts the linear growth rate for $\varepsilon = 4/256$, but gives slightly lower w than $\mathcal{M}_2$ for larger ε. The reason for this behavior is not directly apparent, but it is most likely due to the lack of a consistent level set based interpolation step to calculate the vortex sheet induced velocity $\mathbf{u}$, Eq. (52). Increasing ε results in a consistent reduction of the growth rate for both $\mathcal{M}_2$ and $\mathcal{M}_3$.

In order to further analyze this behavior, Fig. 13 depicts the growth rate w as a function of the shear layer thickness $d = \varepsilon$ in the limit of $We = \infty$ as compared to the analytical solutions, Eqs. (58) and (59). The corresponding numerical values are shown in Table 3. While the qualitative behavior of the simulations and the theory for a linear velocity profile is similar, both velocity methods exhibit overall larger growth rates and hence reach their neutrally stable solution at a larger shear layer thickness of $d \approx 0.8$. This quantitative deviation is due to the different velocity profiles of Eq. (59) and the numerical methods. The former assumes a linear profile, whereas the latter employs a rather complex profile due to the schemes outlined in Section 3.6.2.

Finally, Fig. 14 shows the distribution of the stretching term S and the tension term T along the normalized arc length s/L at $t = 0.5$ calculated with velocity method $\mathcal{M}_2$ and $\varepsilon = 4/256$. For $We = 13$ both terms almost balance, resulting in a small growth rate w. For increasing Weber numbers, the stretching term S starts to dominate the surface tension term T resulting in larger growth rates w. For $We = \infty$ secondary
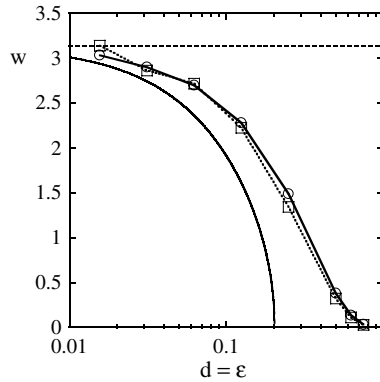
Fig. 13. Growth rate w of the Kelvin–Helmholtz instability in the linear regime as function of the shear layer thickness $d = \varepsilon$, theory for linear velocity profile (——), theory for velocity discontinuity (– – –), velocity methods $\mathcal{M}_2$ (—○—) and $\mathcal{M}_3$ (- -□- -).

Table 3
Linear growth rates w of the Kelvin–Helmholtz instability for varying ε, $We = \infty$, 256×512 grid, methods $\mathcal{M}_2$ and $\mathcal{M}_3$

Method/$d = \varepsilon$	4/256	8/256	16/256	32/256	64/256	128/256	160/256	192/256
Theory Eq. (58)	3.142	3.142	3.142	3.142	3.142	3.142	3.142	3.142
Theory Eq. (59)	2.939	2.742	2.361	1.609	Stable	Stable	Stable	Stable
$\mathcal{M}_2$	3.034	2.899	2.698	2.281	1.489	0.380	0.133	0.032
$\mathcal{M}_3$	3.140	2.863	2.717	2.224	1.342	0.320	0.110	0.026
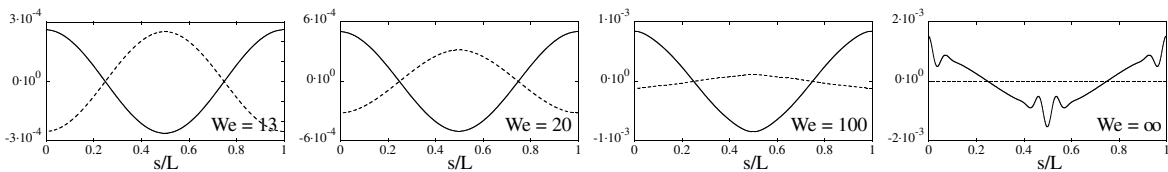
Fig. 14. Stretching term S (solid line) and tension term T (dashed line) at $t = 0.5$, method $\mathcal{M}_2$, $\varepsilon = 4/256$, $We = 13$, $We = 20$, $We = 100$, and $We = \infty$ (from left to right).

instabilities of higher wave number emerge in the distribution of the stretching term, which is consistent with the result reported for the vortex sheet roll-up, cp. Section 4.1.

In conclusion, agreement between the results calculated by the level set/vortex sheet method using any one of the three velocity methods and those obtained from linear theory is very good.

4.3. Long-time evolution of the Kelvin–Helmholtz instability

The evolution of the two-dimensional Kelvin–Helmholtz instability has been studied by a number of authors in the past, see for example [19,22,54]. However, the long-time evolution up to possible topology changes of the interface has been analyzed only by a relatively small number of authors, using a variety of different numerical methods, see [20,55–57].

In the inviscid case, Hou et al. [20] employed marker vortices to track the interface and adaptive methods to approach and resolve singularities in the interface evolution. In the viscous case, Tauber et al. [55] solved the Navier–Stokes equations with an additional source term in the momentum equation to account for sur-

face tension, together with marker points tracking the evolution of the interface. A similar approach has been proposed by Scardovelli and Zaleski [57] employing the Volume-of-Fluid method to track the interface instead.

Here, we will study the long-time evolution of the Kelvin–Helmholtz instability for three different Weber numbers, $We = 20$, 50, and 100. To allow for a direct comparison with the results of Hou et al. [20], their initial conditions are used here, namely Eq. (55) and Eq. (56) with $A_0 = 0.01$ and $\eta^* = -1$. All calculations were performed in a $B \times 2B$ box on an equidistant 256×512 Cartesian grid.

Besides the desingularization discussed in Section 4.1.1, surface tension introduces an additional regularization. Using linear theory, it is easy to show that surface tension forces suppress the growth of higher wave number disturbances [58], cp. also Eq. (58). A detailed discussion of the effect of surface tension on the vortex sheet evolution can for example be found in [54].

4.3.1. We = 20 case

Fig. 15 shows the temporal evolution of the interface shape for $We = 20$ and increasing values of the spreading parameter ε, while Fig. 16 shows the corresponding evolution of the amplitude A of the disturbance. As can be seen, for early times, the amplitude of the disturbance grows rapidly, fastest in the case of the lowest value of ε, and slightly slower for the cases with increased ε. The growth rates are initially higher than linear theory predicts. This is due to the employed initial condition for η that does not take the reduction in growth rate due to surface tension forces into account. As shown in Section 4.2, correcting $\eta(t = 0)$ accordingly results in good agreement with the theoretical linear growth rate. Apart from the difference in amplitudes, the shapes of the interfaces are very similar for varying ε. After the initial fast growth, the interface becomes significantly steeper on the downwind side and finally folds over there, forming fingers stretching into the opposite fluid. At later times, the interface still continues to grow, albeit at a smaller rate.

A similar behavior has been observed in the inviscid simulations of Hou et al. [20]. There, the fingers continue to grow over the midpoint extending ever longer into the opposite fluid. In the viscous simulations
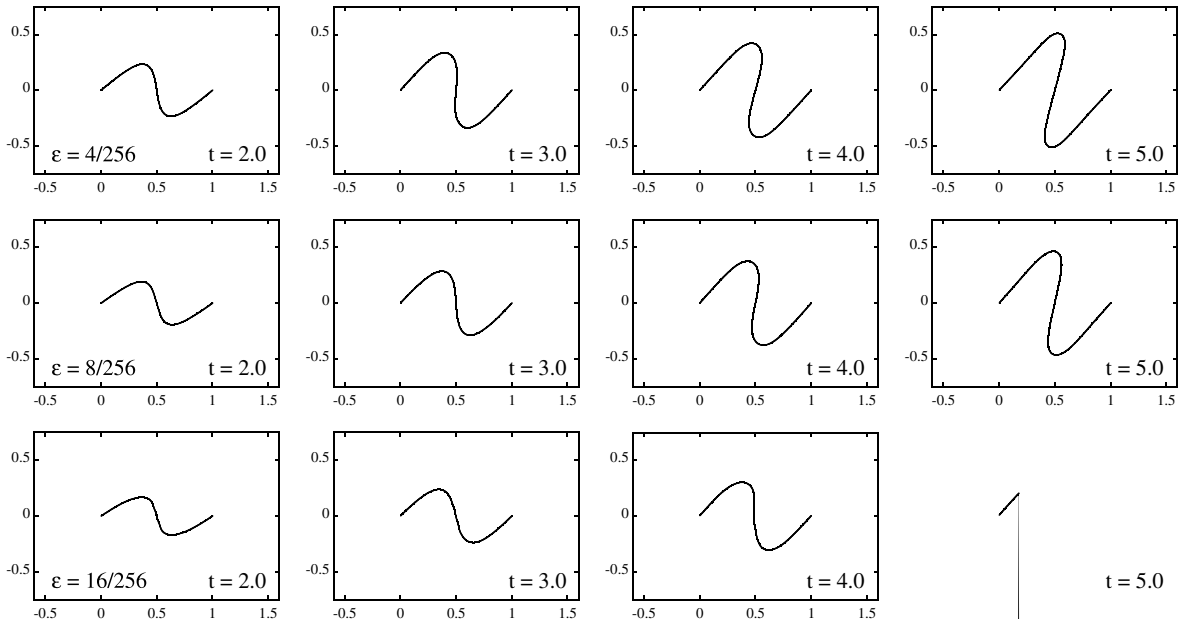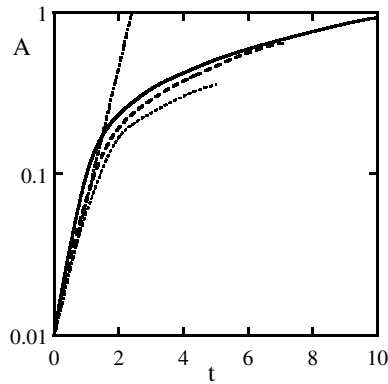
Fig. 16. Temporal evolution of the amplitude for $We = 20$ and spreading parameter $\varepsilon = 4/256$ (solid line), $\varepsilon = 8/256$ (dashed line), $\varepsilon = 16/256$ (dotted line), and linear theory (dashed dotted line).

of Tauber et al. [55] on the other hand, the growth of the interface is eventually stopped and reversed, generating a standing capillarity wave. This is due to the growing shear layer thickness in the presence of viscosity, reducing the effect of stretching so that surface tension starts to dominate. To a certain degree, the presented level set/vortex sheet method falls between these two approaches. Unlike the inviscid method, here, the desingularization introduces a finite shear layer thickness, that is however constant in time and not increasing as in the fully viscous case. Nonetheless, artificially increasing ε, i.e. increasing the shear layer thickness, has a similar effect here as in the fully viscous simulations of Tauber et al. [55] in that the growth rate is decreased, cp. Fig. 16.

Fig. 17 depicts the vortex sheet strength η, the interface curvature κ, the stretching term S, and the tension term T along the interface for $\varepsilon = 8/256$, while Fig. 18 shows the corresponding long-time evolution of the interface shape. As has been reported by both Hou et al. [20] and Tauber et al. [55], the initial single extremum of the vortex sheet strength starts to split up into two extrema located at the tip of the fingers.
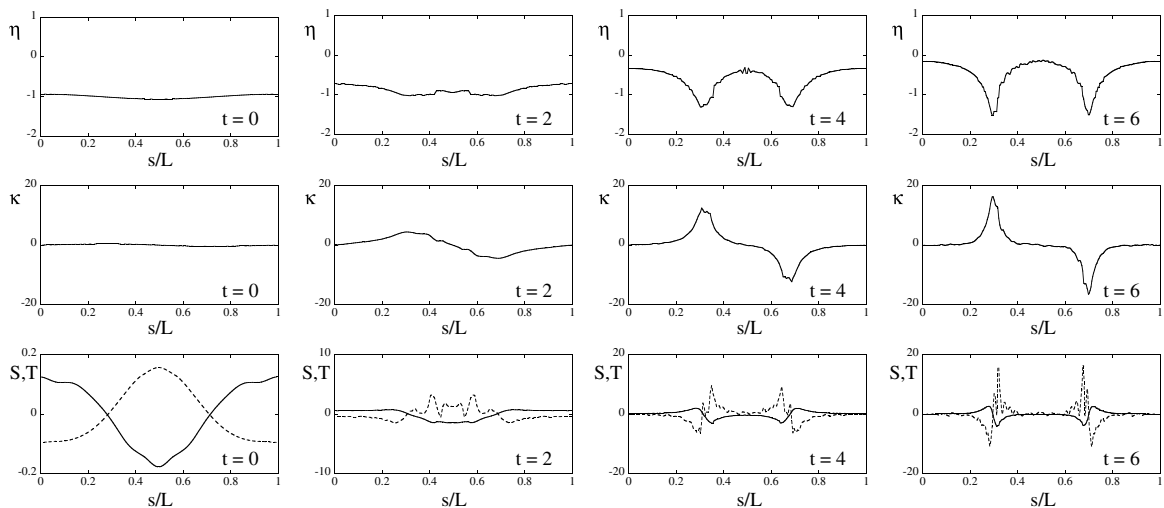

Fig. 17. Vortex sheet strength η (top), curvature κ (middle), stretching term S (solid line, bottom), and tension term T (dashed line, bottom) for $We = 20$ and $\varepsilon = 8/256$ at $t = 0$, 2, 4, and 6.
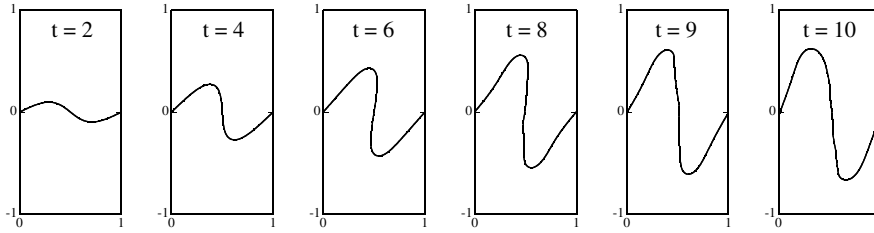
Fig. 18. Interface shape at t = 2, 4, 6, 8, 9, and 10 for We = 20 and ε = 8/256.

These finger tip vortices are however not strong enough to bend the fingers significantly, consistent with the results reported in [20]. Furthermore, surface tension forces are strong enough to prevent the formation of any discontinuity in the curvature distribution. At later times, only the highly curved finger tips are clearly visible in the curvature distribution. Both the stretching term S and tension term T are predominantly located at the finger tips. While the stretching term exhibits a smooth distribution, the tension term shows some local spikes. These appear to be numerical in nature and are most likely due to the numerical scheme used to reinitialize the level set scalar. Alternative numerical schemes that ensure convergence for higher derivatives of the level set scalar, like the recently proposed discontinuous spectral element method for level sets [59], could alleviate this problem.

4.3.2. We = 50 case

The temporal evolution of the interface shape for We = 50 and increasing values of the spreading parameter ε is depicted in Fig. 19, while Fig. 20 shows the corresponding evolution of the amplitude A of the disturbance.
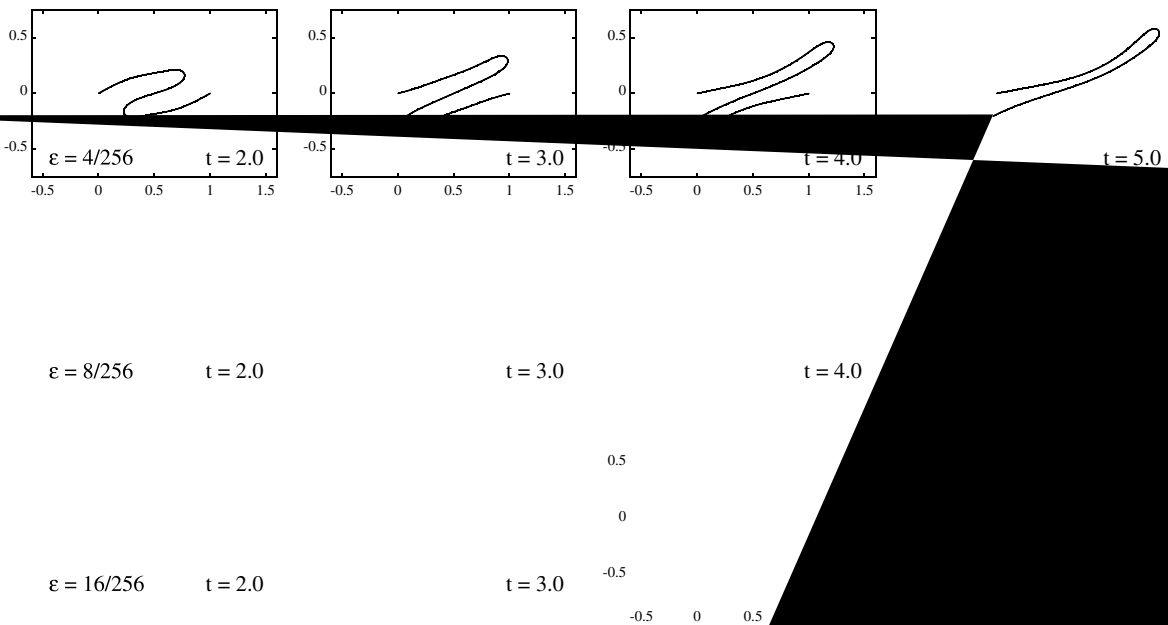

Fig. 19. Influence of the spreading parameter ε for We = 50, t = 2, 3, 4, and 5 (left t[...] row), and ε = 16/256 (bottom row).
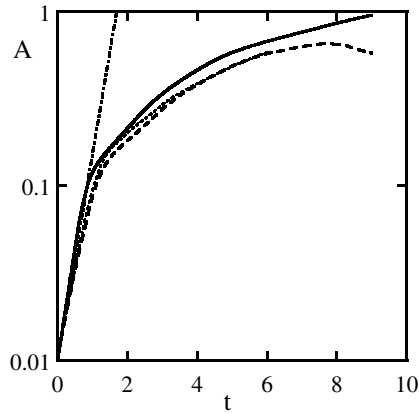
Fig. 20. Temporal evolution of the amplitude for $We = 50$ and spreading parameter $\varepsilon = 4/256$ (solid line), $\varepsilon = 8/256$ (dashed line), $\varepsilon = 16/256$ (dotted line), and linear theory (dashed dotted line).

Again, due to the initial condition for η, the growth rates are slightly higher than linear theory predicts at early times. Following this initial fast growth of the amplitude, the interface quickly folds over and forms two, initially straight, elongated fingers that extend ever further into the opposing fluid. This behavior is in good agreement with the observations of both Hou et al. [20] and Tauber et al. [55]. Varying the spreading parameter ε only has a small effect on the overall shape of the interface. However, decreasing the shear layer thickness by decreasing ε slightly increases the initial growth rate so that at any given time the interface for lower ε extends slightly further into the cross-stream direction.

Fig. 21 depicts the vortex sheet strength η, the interface curvature κ, the stretching term S, and the tension term T along the interface for $\varepsilon = 8/256$, while Fig. 22 shows the corresponding long-time evolution of the interface shape. As is the case for $We = 20$, two maxima in the absolute value of η are observed at the
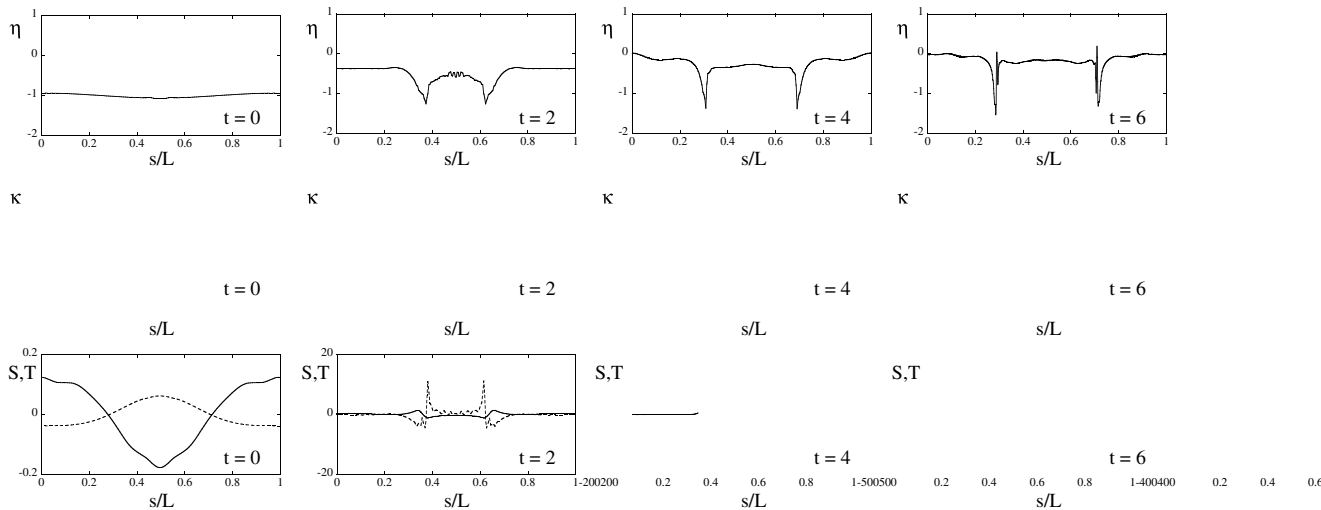

Fig. 21. Vortex sheet strength η (top), curvature κ (middle), stretching term S (solid line, bottom), and tension term T (dashed line, bottom) for $We = 50$ and $\varepsilon = 8/256$ at $t = 0$, 2, 4, and 6.
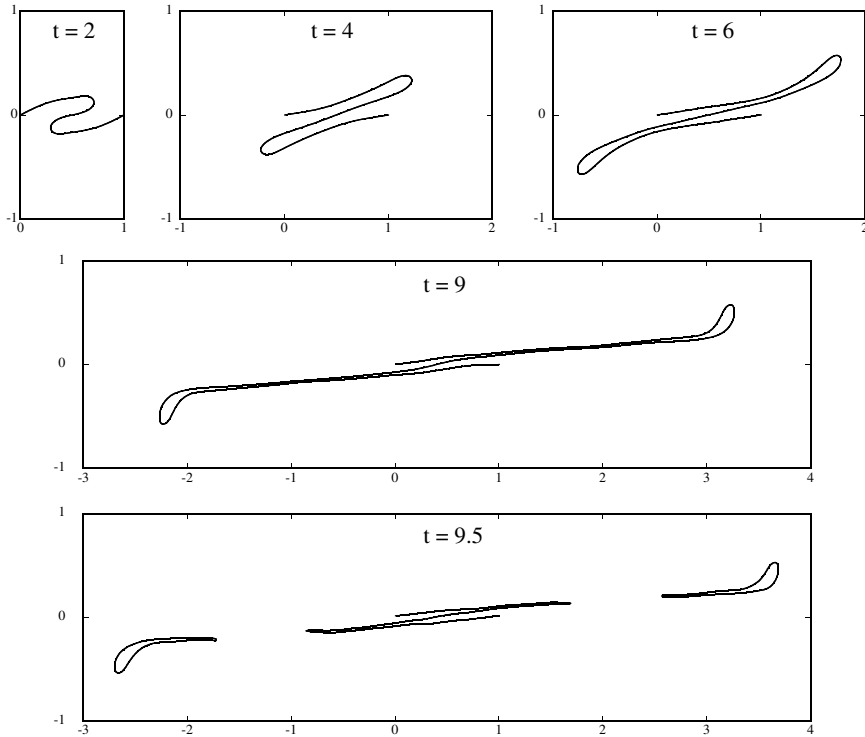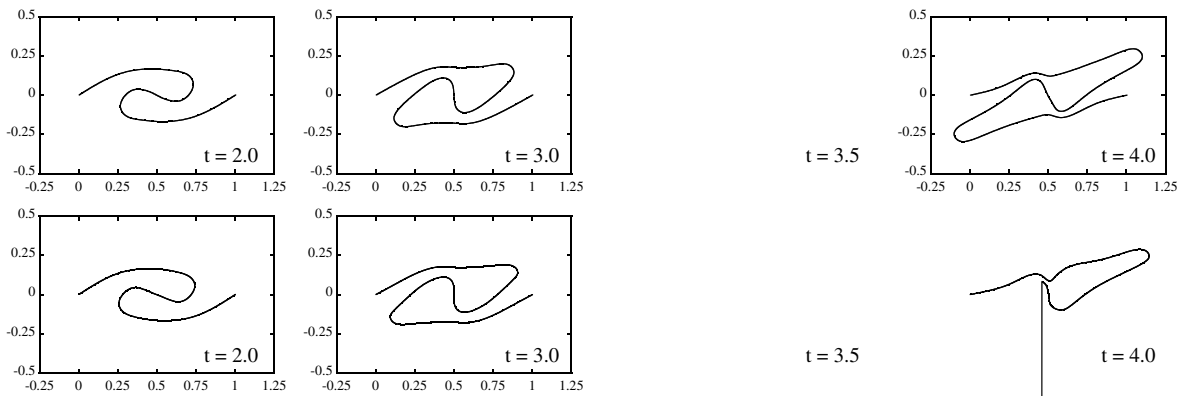
Fig. 22. Interface shape at $t = 2, 4, 6, 9,$ and 9.5 for $We = 50$ and $\varepsilon = 8/256$.

rounded edges of the two fingers. Although the Weber number is larger in this case, the magnitude of the surface tension forces is comparable, because here, both the local curvature and the tangential curvature gradient at the end of the fingers are higher.

For later times, a bulge forms at the finger tips that is significantly bent into the cross stream direction. This tip bending has also been observed by both Hou et al. [20] and Tauber et al. [55], albeit that the bending in [20] is much smaller than the one observed here and in [55]. Furthermore, consistent with the results in [20], the two fingers continue to grow, such that the growth reversal and eventual pull back of the fingers as reported in [55] is not observed here. The behavior reported in [55] is due to the growth of the shear layer thickness, reducing the effect of stretching so that surface tension starts to dominate. Here, however, the shear layer thickness is constant in time, meaning that the ratio of stretching and tension is basically fixed, leading to the observed continual growth of the fingers. At roughly $t = 9.4$, the thin neck is no longer supported by the underlying grid and the neck ruptures. The ruptured ends then quickly retreat, finally forming two drops. Note that this breakup is a numerical effect due to the single valued nature of the level set scalar and the employed numerical grid resolution. If two interface segments enter the same numerical grid cell, breakup takes place automatically. Thus, the employed numerical resolution influences the exact point in time of breakup. Local mesh refinement in conjunction with an additional physical small scale breakup model would have to be used in order to capture the breakup time correctly. This, however, is beyond the scope of the present paper.

4.3.3. We = 100 case

To first ascertain the influence of the employed numerical grid resolution, Fig. 23 shows the temporal evolution of the interface shape for both $B/\Delta x = 128$ and $B/\Delta x = 256$. Obviously, the results are very sim-

0.5 0.25 0 -0.25 -0.5   -0.25 0 0.25 0.5 0.75 1 1.25   t = 2.0

0.5 0.25 0 -0.25 -0.5   -0.25 0 0.25 0.5 0.75 1 1.25   t = 3.0

t = 3.5

0.5 0.25 0 -0.25 -0.5   -0.25 0 0.25 0.5 0.75 1 1.25   t = 4.0

0.5 0.25 0 -0.25 -0.5   -0.25 0 0.25 0.5 0.75 1 1.25   t = 2.0

0.5 0.25 0 -0.25 -0.5   -0.25 0 0.25 0.5 0.75 1 1.25   t = 3.0

t = 3.5

t = 4.0

ilar. Yet, especially at later times, some slight differences can be discerned. These are due to the fact that at later times, the finer grid resolves the small scale structures and hence the curvature and the surface tension forces better.

The temporal evolution of the interface shape for $We = 100$ and increasing values of the spreading parameter ε is depicted in Fig. 24, while Fig. 25 shows the corresponding evolution of the amplitude A of the disturbance. At early times, the interface instability grows roughly according to the results of linear theory. For $We = 100$, the influence of the chosen initial condition for η is not as pronounced as in the $We = 50$ and $We = 20$ cases, because here, the linear growth rate is closest to the $We = \infty$ case used for $\eta(t = 0)$, see Table 2.

Unlike the previous two cases of lower Weber number, here, ε has a large impact on the resulting interface shape. For $\varepsilon = 16/256$, the interface folds over, but does not roll up. The fingers simply continue to
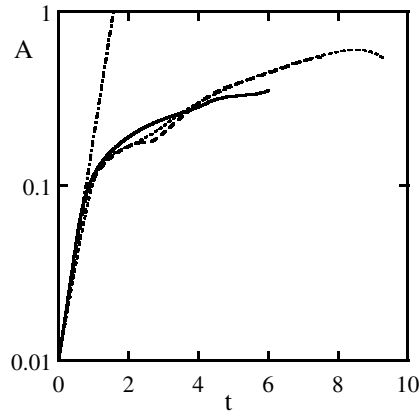
Fig. 25. Temporal evolution of the amplitude for $We = 100$ and spreading parameter $\varepsilon = 4/256$ (solid line), $\varepsilon = 8/256$ (dashed line), $\varepsilon = 16/256$ (dotted line), and linear theory (dashed dotted line).

penetrate into the opposite fluid, because, due to the relatively large shear layer thickness, surface tension is strong enough to prevent the initial roll-up, and the following evolution is similar to the $We = 50$ case.

Decreasing the shear layer thickness by setting $\varepsilon = 8/256$, surface tension is no longer strong enough to prevent the initial roll-up of the interface. Note, however, that the inner part of the interface barely rotates past the vertical, and then quickly starts to unwind for later times, see also Fig. 26. Decreasing
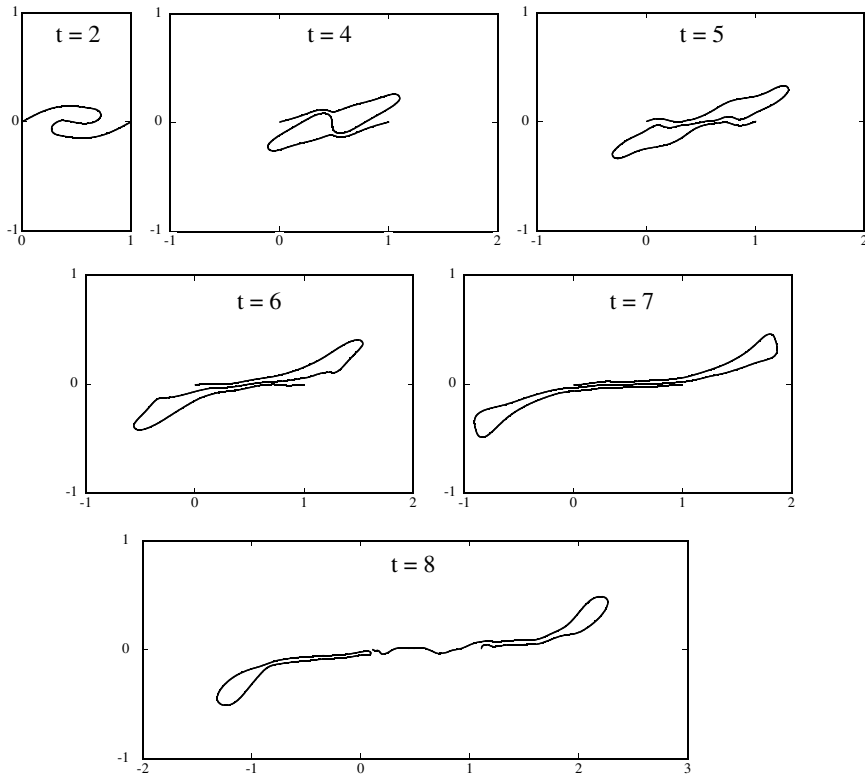

Fig. 26. Interface shape at $t = 2, 4, 5, 6, 7$, and 8 for $We = 100$ and $\varepsilon = 8/256$.

the shear layer thickness even further by setting $\varepsilon = 4/256$, stretching is now strong enough to rotate the inner part of the interface well past the vertical, and the ensuing unwinding is significantly delayed, see Fig. 24. The observed interface geometry in this case is similar to the one observed by Tauber et al. [55]. For both values of ε, two thin "pinching necks" are formed, although neck pinching does not actually occur.

Figs. 27 and 28 show the evolution of the lower "pinching neck" for $\varepsilon = 8/256$ and $\varepsilon = 4/256$ in more detail. The origin in these figures is chosen to coincide with the inner point of the smallest neck distance for each individual time step. At early times, the streamlines are well aligned with the interface and jet-like flows exist in the neck regions leading to a continual decrease in the neck widths as illustrated in Fig. 29. These jets are generated by pairs of positive and negative η at the thinning neck, clearly visible at $t = 4$ in Fig. 30. However, once the central part of the interface starts to unwind in the $\varepsilon = 8/256$ case, the jet breaks down causing the neck width to remain almost constant thereafter, see Fig. 29. At $t = 6$, when the interface has fully unwound, the positive and negative pairs of η have completely disappeared in the former neck region, see Fig. 30. The reason for the unwinding can be seen in the stretching term distribution S at $t = 4$. Apparently, a small amount of positive stretching S that is not sufficiently balanced by tension T, leads to slightly positive values of η in the central part of the interface, causing the local unwinding. Although this has not been observed in the inviscid case by Hou et al. [20], it has been observed in the viscous simulations of Tauber et al. [55], albeit at a later time. In the $\varepsilon = 4/256$ case, the jet in the neck also starts to decrease in strength, but does not entirely disappear, cp. Fig. 28, leading to a continual, albeit very small decrease in the neck width, see Fig. 29.

At later times, the evolution of the amplitude of the stretching fingers for $\varepsilon = 8/256$ and $\varepsilon = 16/256$ coincides very well, cp. Fig. 25. However, the thinning fingers rupture earlier at around $t = 7.9$ in the case of $\varepsilon = 8/256$, see Fig. 26, as compared to $t = 9.3$ for $\varepsilon = 16/256$. In the $\varepsilon = 4/256$ case, the thin fingers leading
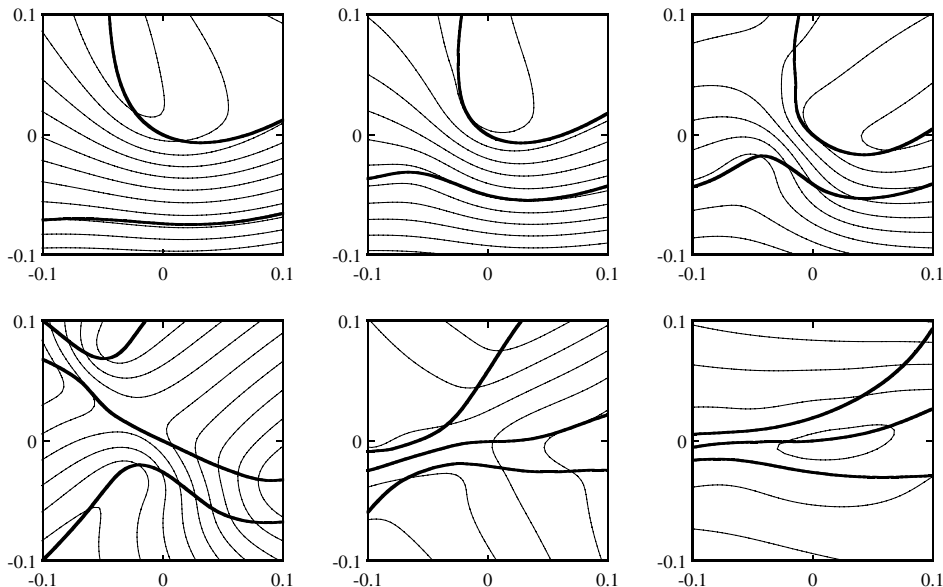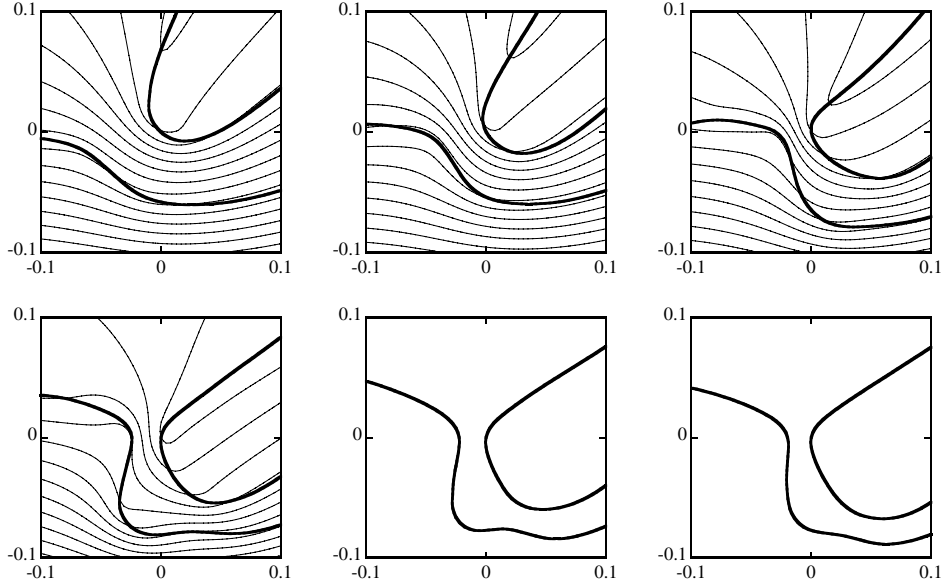

Fig. 27. Interface shape and streamlines at the lower neck at $t = 3, 3.4, 3.8, 4.2, 4.6$, and 5.0 (upper left to lower right) for $We = 100$ and $\varepsilon = 8/256$.

up to the necks rupture just when the unwinding of the central part of the interface sets in. Note, however, that in all three cases, pinching does not occur at the initially formed necks. This is consistent with the results of Tauber et al. [55].

In summary, the formation of the neck pinching singularity as observed in the inviscid simulations of Hou et al. [20] is avoided in the simulations presented here, due to the introduction of a finite shear layer thickness, mimicking the effect of viscosity. The results presented here are thus more in agreement with those presented by Tauber et al. [55] for the fully viscous case.
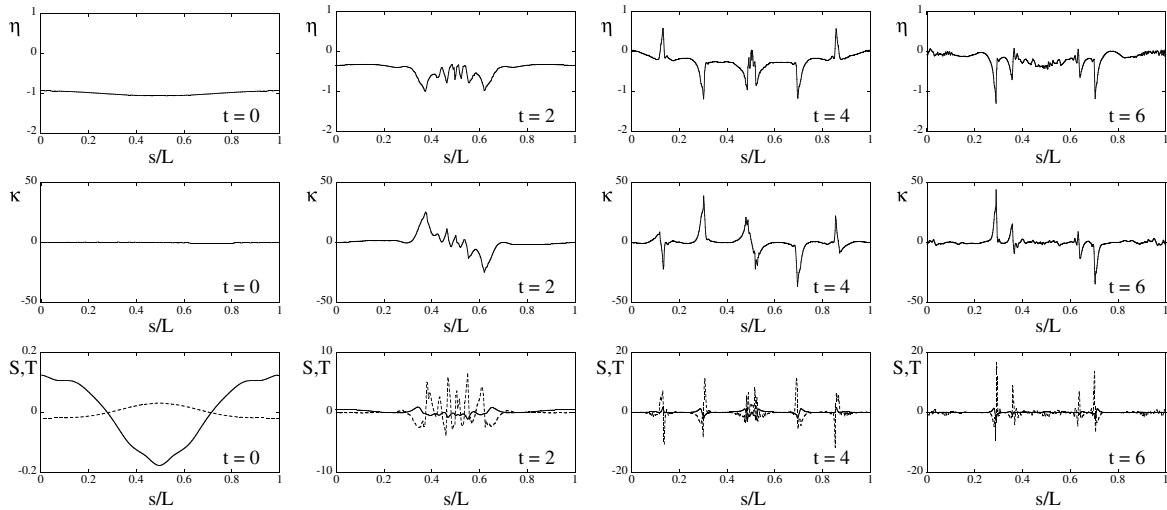
Fig. 30. Vortex sheet strength η (top), curvature κ (middle), stretching term S (solid line, bottom), and tension term T (dashed line, bottom) for $We = 100$ and $\varepsilon = 8/256$ at $t = 0$, 2, 4, and 6.

5. Conclusions

A Eulerian level set/vortex sheet method has been presented that allows for the calculation of the phase interface dynamics between two inviscid fluids of equal density, taking the effect of surface tension forces into account. The extension to three dimensions and fluids of different densities is straightforward. Results calculated with the presented method are comparable to those obtained by Lagrangian vortex particle methods. Furthermore, the calculated growth rates for the Kelvin–Helmholtz instability in the linear regime are in very good agreement with the linear theory. The neck pinching singularity observed in the inviscid case of the long-time evolution of the Kelvin–Helmholtz instability for larger Weber numbers [20] is not observed here. This is due to the desingularization introduced by the spreading parameter ε, that effectively fixes the local shear layer thickness to a finite value, thereby mimicking the effect of viscosity. The calculated results are thus more in agreement with those reported for the viscous case [55]. Since the phase interface location and motion are represented by a level set approach, topology changes of the interface, like breakup and merging, are handled automatically. The main advantage of the presented method is the fact that it allows for the direct study of the physical processes at the phase interface itself, specifically stretching and surface tension effects.

Acknowledgement

References

[1] P.J. O'Rourke, Collective drop effects on vaporizing liquid sprays, Ph.D. Thesis, vol. 1532-T, Princeton University, 1981.
[2] P.J. O'Rourke, A.A. Amsden, The TAB method for numerical calculations of spray droplet breakup, Tech. Rep. 872089, SAE Technical Paper, 1987.

[3] R.D. Reitz, Modeling atomization processes in high-pressure vaporizing sprays, Atom. Spray Tech. 3 (1987) 309–337.

[4] R.D. Reitz, R. Diwakar, Structure of high pressure fuel sprays, Tech. Rep. 870598, SAE Technical Paper, 1987.

[5] F.X. Tanner, Liquid jet atomization and droplet breakup modeling of non-evaporating Diesel fuel sprays, SAE Trans.: J. Engines 106 (3) (1997) 127–140.

[6] J.U. Brackbill, D.B. Kothe, C. Zemach, A continuum method for modeling surface tension, J. Comput. Phys. 100 (1992) 335–354.

[7] J.U. Brackbill, D.B. Kothe, H.M. Ruppel, FLIP: A low dissipation, particle-in-cell method for fluid flow, Comput. Phys. Commun. 48 (1988) 25–38.

[8] W.J. Rider, D.B. Kothe, Stretching and tearing interface tracking methods, Tech. Rep., Los Alamos National Laboratory, AIAA Paper 95-1717, 1995.

[9] S.O. Unverdi, G. Tryggvason, A front-tracking method for viscous, incompressible, multi-fluid flows, J. Comput. Phys. 100 (1992) 25–37.

[10] W.F. Noh, P. Woodward, SLIC (simple line interface calculation), in: A.I.V.D. Vooren, P.J. Zandenbergen (Eds.), Lecture Notes in Physics, Proceedings of the Fifth International Conference on Numerical Methods in Fluid Dynamics, Vol. 59, Springer, Berlin, 1976, pp. 330–340.

[11] D.B. Kothe, W.J. Rider, Comments on modelling interfacial flows with Volume-of-Fluid methods, Tech. Rep. LA-UR-3384, Los Alamos National Laboratory, 1995.

[12] D. Gueyffier, J. Li, A. Nadim, S. Scardovelli, S. Zaleski, Volume of fluid interface tracking with smoothed surface stress methods for three-dimensional flows, J. Comput. Phys. 152 (1999) 423–456.

[13] S. Osher, J.A. Sethian, Fronts propagating with curvature-dependent speed: algorithms based on Hamilton–Jacobi formulations, J. Comput. Phys. 79 (1988) 12–49.

[14] M. Sussman, P. Smereka, S. Osher, A level set method for computing solutions to incompressible two-phase flow, J. Comput. Phys. 119 (1994) 146.

[15] M. Sussman, E. Fatemi, P. Smereka, S. Osher, An improved level set method for incompressible two-phase flows, Comput. Fluids 27 (5–6) (1998) 663–680.

[16] M. Brocchini, D.H. Peregrine, The dynamics of strong turbulence at free surfaces. Part 1. Description, J. Fluid Mech. 449 (2001) 225–254.

[17] M. Brocchini, D.H. Peregrine, The dynamics of strong turbulence at free surfaces. Part 2. Free-surface boundary conditions, J. Fluid Mech. 449 (2001) 255–290.

[18] G.R. Baker, D.I. Meiron, S.A. Orszag, Generalized vortex methods for free-surface flow problems, J. Fluid Mech. 123 (1982) 477–501.

[19] D.I. Pullin, Numerical studies of surface-tension effects in nonlinear Kelvin–Helmholtz and Rayleigh–Taylor instability, J. Fluid Mech. 119 (1982) 507–532.

[20] T.Y. Hou, J.S. Lowengrub, M.J. Shelley, The long-time motion of vortex sheets with surface tension, Phys. Fluids 9 (7) (1997) 1933–1954.

[21] T.Y. Hou, J.S. Lowengrub, M.J. Shelley, Boundary integral methods for multicomponent fluids and multiphase materials, J. Comput. Phys. 169 (2001) 302–362.

[22] R.H. Rangel, W.A. Sirignano, Nonlinear growth of Kelvin–Helmholtz instability: effect of surface tension and density ratio, Phys. Fluids 31 (7) (1988) 1845–1855.

[23] N. Peters, The turbulent burning velocity for large-scale and small-scale turbulence, J. Fluid Mech. 384 (1999) 107–132.

[24] N. Peters, Turbulent Combustion, Cambridge University Press, Cambridge, UK, 2000.

[25] E. Harabetian, S. Osher, C.W. Shu, An Eulerian approach for vortex motion using a level set regularization procedure, J. Comput. Phys. 127 (1996) 15–26.

[26] D. Peng, B. Merriman, S. Osher, H. Zhao, M. Kang, A PDE-based fast local level set method, J. Comput. Phys. 155 (1999) 410–438.

[27] P.G. Saffman, G.R. Baker, Vortex interactions, Annu. Rev. Fluid Mech. 11 (1979) 95.

[28] T.Y. Hou, J.S. Lowengrub, M.J. Shelley, Removing the stiffness from interfacial flows with surface tension, J. Comput. Phys. 114 (1994) 312–338.

[29] E. Harabetian, S. Osher, Regularization of ill-posed problems via the level set approach, SIAM J. Appl. Math. 58 (6) (1998) 1689–1706.

[30] L.M. Milne-Thomson, Theoretical Hydrodynamics, MacMillan, New York, 1968.

[31] R. Krasny, Desingularization of periodic vortex sheet roll-up, J. Comput. Phys. 65 (1986) 292–313.

[32] J.P. Christiansen, Numerical simulation of hydrodynamics by the method of point vortices, J. Comput. Phys. 13 (1973) 363–379.

[33] G.-H. Cottet, P.D. Koumoutsakos, Vortex Methods, Cambridge University Press, Cambridge, 2000.

[34] G.-S. Jiang, D. Peng, Weighted ENO schemes for Hamilton–Jacobi equations, SIAM J. Sci. Comput. 21 (6) (2000) 2126–2143.

[35] C.W. Shu, S. Osher, Efficient implementation of essentially non-oscillatory shock-capturing schemes, II, J. Comput. Phys. 83 (1989) 32–78.

[36] S. Osher, C.W. Shu, High-order essentially nonoscillatory schemes for Hamilton–Jacobi equations, SIAM J. Numer. Anal. 28 (4) (1991) 907–922.

[37] C.W. Shu, Total-variation-diminishing time discretization, SIAM J. Sci. Statist. Comput. 9 (6) (1988) 1073–1084.

[38] M. Sussman, E. Fatemi, An efficient, interface-preserving level set redistancing algorithm and its application to interfacial incompressible fluid flow, SIAM J. Sci. Comput. 20 (4) (1999) 1165–1191.

[39] D. Enright, R. Fedkiw, J. Ferziger, I. Mitchell, A hybrid particle level set method for improved interface capturing, J. Comput. Phys. 183 (2002) 83–116.

[40] J.A. Sethian, Fast marching methods, SIAM Rev. 41 (2) (1999) 199–235.

[41] D. Adalsteinsson, J.A. Sethian, The fast construction of extension velocities in level set methods, J. Comput. Phys. 148 (1999) 2–22.

[42] A.B. Ebiana, R.W. Bartholomew, Design considerations for numerical filters used in vortex-in-cell algorithms, Comput. Fluids 25 (1) (1996) 61–75.

[43] C.S. Peskin, Numerical analysis of blood flow in the heart, J. Comput. Phys. 25 (1977) 220–252.

[44] P. Swarztrauber, R. Sweet, Efficient FORTRAN subprograms for the solution of elliptic partial differential equations, Tech. Rep. NCAR Technical Note-TN/IA-109, NCAR, July 1975.

[45] D.W. Moore, The spontaneous appearance of a singularity in the shape of an evolving vortex sheet, Proc. Roy. Soc. London A 365 (1979) 105–119.

[46] G. Tryggvason, W.J.A. Dahm, K. Sbeih, Fine structure of vortex sheet rollup by viscous and inviscid simulation, J. Fluids Eng. 113 (1991) 31–36.

[47] D.I. Meiron, G.R. Baker, S.A. Orszag, Analytic structure of vortex sheet dynamics. Part 1. Kelvin–Helmholtz instability, J. Fluid Mech. 114 (1982) 283–298.

[48] M.J. Shelley, A study of singularity formation in vortex-sheet motion by a spectrally accurate vortex method, J. Fluid Mech. 244 (1992) 493–526.

[49] L. Rayleigh, On the stability, or instability, of certain fluid motions, Proc. London Math. Soc. 11 (1880) 57–70.

[50] H.V. Helmholtz, On discontinuous movements of fluids, Philos. Mag. 36 (1868) 337–346.

[51] L. Kelvin, Hydrokinetic solutions and observations, Philos. Mag. 42 (1871) 362–377.

[52] A. Michalke, On the inviscid instability of the hyperbolic-tangent velocity profile, J. Fluid Mech. 19 (1964) 543–556.

[53] P. Yecko, S. Zaleski, J.-M. Fullana, Viscous modes in two-phase mixing layers, Phys. Fluids 14 (12) (2002) 4115–4122.

[54] G. Baker, A. Nachbin, Stable methods for vortex sheet motion in the presence of surface tension, J. Sci. Comput. 19 (1998) 1737–1766.

[55] W. Tauber, S.O. Unverdi, G. Tryggvason, The nonlinear behaviour of a sheared immiscible fluid interface, Phys. Fluids 14 (8) (2002) 2871–2885.

[56] J. Li, E. Lopez-Pages, P. Yecko, S. Zaleski, Droplet formation in sheared liquid–gas layers, http://citeseer.ist.psu.edu/561899.html, (2004).

[57] R. Scardovelli, S. Zaleski, Direct numerical simulation of free-surface and interfacial flow, Annu. Rev. Fluid Mech. 31 (1999) 567–603.

[58] S. Chandrasekhar, Hydrodynamic and Hydromagnetic Stability, Oxford University Press, London, 1961.

[59] M. Sussman, M.Y. Hussaini, A discontinuous spectral element method for the level set equation, J. Sci. Comput. 19 (2003) 479–500.